Available online at www.sciencedirect.com
ScienceDirect
Comput. Methods Appl. Mech. Engrg. 410 (2023) 115962
Computer methods in applied mechanics and engineering
www.elsevier.com/locate/cma

Phase-field modeling of drying-induced cracks: Choice of coupling and study of homogeneous and localized damage

Chenyi Luo[a], Lorenzo Sanavia[b], Laura De Lorenzis[a,*]

[a] *Eidgenossische Technische Hochschule Zurich, Switzerland*
[b] *University of Padua, Italy*

Received 6 January 2023; received in revised form 10 February 2023; accepted 14 February 2023
Available online xxxx

Abstract

Phase-field modeling has already proved to be a suitable framework to predict the initiation and propagation of drying cracks in variably saturated porous media. In this paper, we focus on some fundamental modeling aspects which have not yet been given sufficient attention. In the first part, different formulations for the total energy, characterized by different choices for the coupling between the damage and the poro-mechanical fields, are evaluated based on their ability to lead to qualitatively reasonable predictions for two benchmark cases of free and restrained desiccation. In the second part, for a selected energy formulation, we conduct the variational analysis of the quasi-static damage evolution. Hereby, we focus on restrained desiccation under a given capillary pressure distribution, resulting from the solution of Richards equation with either flux-driven or pressure-driven boundary conditions. Extending the analysis in Sicsic et al. (2014) to the present case, we show that the damage evolution follows first a fundamental branch without localization, and then bifurcates into another branch with damage localization, which leads to the initiation of periodic cracks. The analysis enables the computation of the drying crack spacing as a function of material and loading parameters.

Keywords: Phase-field modeling; Desiccation cracks; Drying cracks; Period cracking; Brittle fracture

1. Introduction

The process of desiccation- or drying-induced cracking in porous media is ubiquitous in natural and man-made materials alike. It has been observed e.g. in clayey soils [1], blood [2], and hydrogels [3], among many others. Its investigation is motivated by the need to understand the underlying mechanisms, characterize the crack patterns, and control the crack development [4].

The process is very complex, as it involves the deformation of the solid skeleton, the capillary action between the solid and the fluids and the phase transitions (mainly evaporation of the in-pore fluid). Experimental studies, from microscale observations to field inspections, provided qualitative understanding of many aspects of the process, including influential factors, distinct stages, and crack patterns, see the recent review in [5]. It was found that cracking is sensitive to boundary conditions [6]; for example, in clayey soils, cracks will be generated during

* Corresponding author.
E-mail address: ldelorenzis@ethz.ch (L. De Lorenzis).

https://doi.org/10.1016/j.cma.2023.115962

drying if the boundaries are restrained, see e.g. [1,7,5,8]. Cracking also depends on drying rate, layer thickness and initial moisture content [9], flaws and small variations in strength of the material [10], and drying–wetting cycles [11,12]. Most desiccation cracks are found to arise in opening mode [13] but cracks in mixed sliding and opening modes are also observed [14,15]. Cracks are typically seen to initiate when the porous media is still (nearly) fully saturated [16,17]. Finally, a large number of more or less equally spaced cracks are formed in elongated, beam-like specimens, while a network of complex intersecting cracks is observed in square or rectangular slabs [18].

Modeling and simulation of desiccation cracking were pursued to interpret the experimental results and shed light on the key phenomena under various scenarios. A comprehensive review of the available approaches is not attempted here and can be found e.g. in [5]. As follows, we just highlight a few main categories of contributions based on continuum mechanical modeling and numerical discretization. The simplest approaches ignore hydro-mechanical coupling and prescribe an evaporation-induced shrinkage strain, leading to cracking in the solid skeleton, see e.g. [19]. Other investigations propose coupled hydro-mechanical models but do not incorporate cracking. E.g., the model in [20] considers linear moisture diffusion coupled to elasticity and can predict the evolution of moisture content and deformation up to initiation of the first crack. The more complex model in [21] is based on a multi-phase and multi-species approach considering the interplay of solid, liquid and gas; once again results are meaningful up to crack initiation. More recent contributions account for both hydro-mechanical coupling and fracture. The approaches to deal with cracks in the discretized setting range from lattice representations with strength criteria [22], to interface elements within finite element analyses, where the interfaces feature strength criteria [23,24] or cohesive behavior [25–27], to finite elements with embedded cracks [28].

Computational approaches for desiccation fracture inherit the difficulties of the underlying methods to deal with cracks, including the need for explicit or implicit tracking of the discontinuities (a tedious task especially in three dimensions), the need for ad hoc criteria to handle initiation and any topological change of the crack surfaces such as merging or branching and the need for contact formulations to deal with crack face interpenetration in compression. The variational phase-field approach to fracture, pioneered in [29] as the regularization of Francfort and Marigo's variational fracture formulation [30] and later recovered as a special family of gradient damage models [31,32], provides a natural solution to the above difficulties. The computational framework enabled by the variational phase-field formulation naturally encompasses both nucleation and propagation, and is able to handle crack topology of arbitrary complexity in two and three dimensions, with no need for crack tracking procedures or for ad hoc criteria to guide the occurrence of complicated changes in the crack topology. Due to these advantages, the formulation gained wide application in various fields [33,34].

In standard phase-field models [29], the damage behavior is symmetric in tension and compression. More complex models have been developed to avoid crack interpenetration in compression and to obtain an asymmetric behavior in tension and compression as observed in experiments. The most widely used of these models [35,36], see also [37] for a review, include the decomposition (also denoted as split) of the strain energy density into active and inactive parts, the first one considered responsible for driving the damage. E.g. in the model by Amor et al. [35], a deviatoric–volumetric split is chosen and damage is driven by the deviatoric strain energy and by the volumetric strain energy associated to positive volumetric strain; in the split by Miehe et al. [36], a spectral decomposition of the strain tensor is performed, and damage is only driven by the contributions with positive eigenvalues. The performance of both models for several benchmark tests is compared in [33]. The development of a more flexible energy decomposition is still an active field of research [37,38].

In the context of cracking in multiphase porous materials with phase-field models, the early research mainly focuses on hydraulic fracturing in saturated porous media, e.g. [39–41], where cracks are triggered by a fluid injection. In early attempts to simulate drying-induced cracks, the effect of drying is modeled by applying a pre-defined tensile isotropic inelastic strain and the phase-field approach successfully replicates crack patterns of colloidal suspensions in unidirectional drying [42]. In [43], the coupling between solid deformation and moisture content is considered analogous to the thermo-mechanical coupling induced by thermal expansion; consequently, the phase-field variable is coupled to the mechanics through the total stress, as opposed to the coupling via the effective stress formulated by the same authors for the case of hydraulic fracture. In [44], the governing equations for isothermal variably saturated porous media are coupled with the evolution equation for the phase-field variable, whereby coupling is performed through the effective stress. In [45], two different energies are proposed for desiccation- and hydraulic fracture, and coupling is performed via the total and the effective stress for the two cases, respectively. However, the approach is non-variational, hence the stress and the damage criterion are not derived

from the variational derivative of the same energy functional. A recent variational approach is proposed in [46], leading to a phase-field model associated with the degradation of the retention properties of the porous medium. The strain energy decomposition models also vary among these works. In the earlier papers [39,40,42], no split of the strain energy density is introduced; the deviatoric–volumetric split is adopted in [44,45] while the spectral decomposition is chosen in [41,43]. No fundamental analysis appears to have been carried out thus far regarding the influence of different coupling choices and energy decompositions on the capability of a variational phase-field model to realistically describe desiccation cracking, at least qualitatively.

One major advantage of the phase-field framework over some of the alternative approaches is that crack initiation and propagation can both be captured seamlessly. Nucleation of a crack is identified with the localization of the phase-field variable. When considering local minimization as a criterion to select the stable states during a quasi-static evolution, localization events are associated to the loss of the stability of the so-called homogeneous solution, i.e. the solution featuring a uniform damage level. The corresponding nucleation load is the one at which the current solution branch ceases to be a local minimum of the energy [31,32,47]. The simplest analysis relying on this approach determines the failure load of a one-dimensional bar under tension and studies the transition between an initial solution with homogeneous damage and a bifurcated branch with a localized solution. Issues of uniqueness and stability for this case are investigated in [47–49]. In more complex problems, multiple cracks may be triggered at the same time, sometimes forming a periodic array, such as in thermal shocks and in desiccation cracking [50,51] (note that, at the end of desiccation, the cracks form a network similar to thermal shock networks [8]). Capturing these complex solutions can take full advantage of the flexibility of the phase-field approach.

Thus far, a fundamental analysis of the nucleation of an array of cracks within the phase-field modeling framework has only been carried out for the thermal shock problem [51], departing from the analytical solution of the heat equation for a constant thermal drop on the free surface of a two-dimensional semi-infinite domain. The analysis reveals that, if a sufficiently large temperature difference is applied, damage immediately takes place. In an initial phase, the solution for both the displacement and the damage variable is homogeneous in the direction parallel to the free surface. Later on, bifurcation occurs to a periodic solution, which suggests the initiation of multiple parallel cracks. It is reasonable to expect that qualitatively similar results can be found from the analysis of a desiccation problem. However, some additional complications arise in this case, due to the lack of an analytical solution, the more complex role played by hydraulic boundary conditions, and the wider range of possibilities for the choice of the governing energy functional, as hinted to above.

In this work, we focus on the variational phase-field modeling of desiccation cracking in initially water-saturated clayey soils. In the first part of the paper, we aim to address the consequences of different coupling choices in the energy functional at the basis of the approach. Possible formulations for the total energy, characterized by different choices for the coupling between the damage and the poro-mechanical fields, are summarized into two model families. Then, they are evaluated based on their ability to lead to qualitatively reasonable predictions for two benchmark cases, i.e. free and restrained desiccation. In the second part of the paper, inspired by the work of Sicsic et al. [52], we carry out a semi-analytical study to evaluate the fundamental behavior of the phase-field models selected from the previous evaluation. Hereby, we focus on restrained desiccation and conduct the stability analysis of the quasi-static damage evolution, where the pore pressure is pre-derived by solving the Richards equation under either flux-driven or pressure-driven boundary conditions.

The remainder of this paper is structured as follows. The hydraulic problem for unsaturated soils is first briefly introduced in Section 2. In Section 3, the free energy for an undamaged porous solid is expressed in two formats, which inspire the formulation of two variational model families for the porous solid with damage. In Section 4, these model families are evaluated on two simple setups, namely free and restrained drying, with respect to their capability to qualitatively reproduce the expected behavior. Section 5 presents the analysis of the homogeneous damaging phase and of the subsequent bifurcation, leading to the initiation of an array of cracks. Conclusions are drawn in Section 6.

As follows, we report a brief overview of the notation. Vectors and second-order tensors are both denoted by boldface fonts, e.g. $\mathbf{u}$ and $\boldsymbol{\varepsilon}$ for the displacement vector and strain tensor. Given a scalar valued function $f : x \to f(x) \in \mathbb{R}$, we define its positive and negative parts as

$$\langle f(x)\rangle_+ = \frac{f(x)}{2} + \frac{|f(x)|}{2}, \quad \langle f(x)\rangle_- = \frac{f(x)}{2} - \frac{|f(x)|}{2}. \tag{1}$$

The Heaviside function is defined as

$$H(x) = \begin{cases} 1, & \text{if } x > 0 \\ 0, & \text{if } x \leq 0 \end{cases} \tag{2}$$

For functions depending on one variable, a prime symbol denotes the first derivative with respect to that variable, e.g. $A'(\alpha) = \frac{\mathrm{d}A}{\mathrm{d}\alpha}$.

2. The hydraulic problem for variably saturated porous media

In the formulation adopted in this paper, we consider linearly elastic porous materials and treat them as multi-phase continua with the pores of the solid skeleton filled by liquid water and air. Considering the small thickness of the samples tested in laboratories when studying desiccation cracking, air is assumed at constant atmospheric pressure and negligible density (as per the so-called passive air phase assumption [53]). This implies also that in the partially saturated zones the sorption equilibrium equation (e.g. [53]) reduces to $p_c = -p_{rw}$, where p_c is the capillary pressure and p_{rw} the water pressure relative to the atmospheric pressure. For simplicity, this variable is further indicated as p_w. This equation states that capillary pressure can be approximated as negative water pressure (or pore water traction).

2.1. Governing equations

As follows, we briefly recall the governing equations of the hydraulic problem considered uncoupled from the mechanical problem and in absence of damage. This uncoupled setting will enable our semi-analytical derivations at a later stage. Let us consider a body $\Omega \subset \mathbb{R}^d$, with d (equal to 2 or 3) as the number of space dimensions, made of a variably saturated porous material whose current hydraulic state is characterized by its water pressure $p_w : \mathbf{x} \in \mathbb{R}^d, t \in \mathbb{R}^+ \rightarrow p_w(\mathbf{x}, t) \in \mathbb{R}$. Within the bulk of the domain, the mass balance equation of the pore water can be expressed as

$$\frac{\partial}{\partial t}(\phi S_w) + \mathrm{div}\mathbf{q} = 0. \tag{3}$$

In this equation, $\phi(\mathbf{x}, t)$ is the Lagrangian porosity, $S_w(\mathbf{x}, t)$ the water degree of saturation, and $\mathbf{q}(\mathbf{x}, t)$ represents the filtration water velocity. The latter is related to the water pressure by the linear momentum balance equation for the water, which, in the quasi-static case, amounts to Darcy's law,

$$\mathbf{q} = \frac{k_L k_r}{\rho_w g}(-\nabla p_w + \rho_w \mathbf{g}) = k\left(-\nabla h + \frac{\mathbf{g}}{g}\right) \tag{4}$$

where $k_L(\mathbf{x}, t)$ is the hydraulic conductivity in saturated conditions, $k_r(\mathbf{x}, t)$ the relative permeability, $k = k_L k_r$ the hydraulic conductivity in variably saturated conditions, ρ_w the water density, assumed constant, $\mathbf{g}$ the gravity acceleration with magnitude g, and $h(\mathbf{x}, t) = p_w/(\rho_w g)$ the pressure head. The combination of Eqs. (3) and (4) gives

$$\frac{\partial}{\partial t}\left(\phi^0 S_w\right) + \mathrm{div}\left[k\left(-\nabla h + \frac{\mathbf{g}}{g}\right)\right] = 0, \tag{5}$$

where we have taken $\phi \simeq \phi^0$ with ϕ^0 as the initial porosity.[1] Note that $S_w(\mathbf{x}, t)$ and $k_r(\mathbf{x}, t)$ (hence $k(\mathbf{x}, t)$) are non-linear functions of $h(\mathbf{x}, t)$. Thus Eq. (5), which is also known as the Richards equation, is a non-linear partial

[1] In general, the Lagrangian porosity ϕ in Eq. (3) depends on the deformation of the porous solid through

$$\phi = \phi^0 + b\left(\epsilon - \epsilon^0\right) + \frac{1}{N}\left(\Pi - \Pi^0\right),$$

in which ϕ^0 is the initial porosity, $\epsilon = \mathrm{tr}(\boldsymbol{\varepsilon})$ is the trace of the infinitesimal solid strain tensor $\boldsymbol{\varepsilon}$ with initial value ϵ^0, Π is the effective pore pressure (to be introduced later) with initial value Π^0, and b and N are material properties known as Biot's coefficient and Biot's modulus, respectively [54,55]. For soils, it is commonly accepted that $b \simeq 1$ and $N \rightarrow \infty$, so that the previous constitutive equation simplifies to

$$\phi = \phi^0 + \epsilon - \epsilon^0 \qquad \text{or} \qquad \varphi = \epsilon - \epsilon^0$$

with $\varphi = \phi - \phi^0$. If the solid is rigid or the volumetric strain of the solid is very small compared to the porosity, we can assume $\phi \simeq \phi^0$ and there is no coupling between the pressure and the deformation.

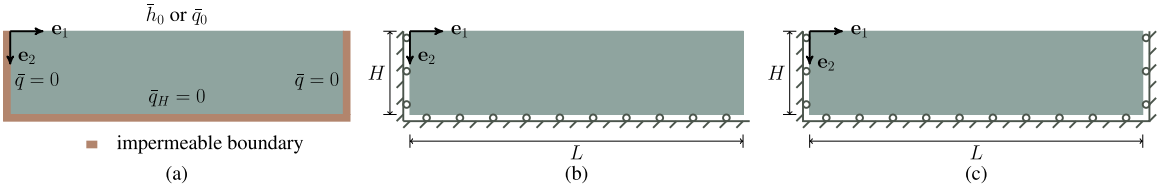

Fig. 1. Setup of the (a) hydraulic problem, (b) free desiccation and (c) restrained desiccation examples.

differential equation in the unknown function h (or, equivalently, p_w). Using the chain rule, we can rewrite (5) as

$$C(h)\frac{\partial h}{\partial t} = \operatorname{div}\left[k(h)\left(\nabla h - \frac{\mathbf{g}}{g}\right)\right] \tag{6}$$

with $k(h) = k_L k_r(h)$ and $C(h) = \phi^0 \frac{\partial S_w}{\partial h}$.

For the closure of the model, we adopt the van Genuchten constitutive equations [56], which relate the saturation and relative permeability to the pressure head as follows,

$$S_w(h) = \begin{cases} 1 & h \geq 0 \\ (1 - S_r)\, S_e(h) + S_r & h < 0 \end{cases} \tag{7}$$

and

$$k_r(h) = \begin{cases} 1 & h \geq 0, \\ \sqrt{S_e(h)}\left[1 - \left(1 - S_e^{1/m_{vG}}(h)\right)^{m_{vG}}\right]^2 & h < 0, \end{cases} \tag{8}$$

where the effective saturation $S_e(\mathbf{x}, t)$ is given by

$$S_e(h) = \left[1 + (-\alpha_{vG} h)^{n_{vG}}\right]^{-m_{vG}} \tag{9}$$

with $m_{vG} = 1 - 1/n_{vG}$. It follows that

$$C(h) = \phi^0 \frac{\partial S_w}{\partial h} = \begin{cases} 0 & h \geq 0, \\ \phi^0 (1 - S_r)\, m_{vG} n_{vG} \alpha_{vG} \left[1 + (-\alpha_{vG} h)^{n_{vG}}\right]^{-m_{vG}-1} (-\alpha_{vG} h)^{n_{vG}-1} & h < 0. \end{cases} \tag{10}$$

The residual saturation S_r and the van Genuchten constants α_{vG} and n_{vG} are hydraulic constitutive parameters to be determined by experiments.

Finally, we need to specify the boundary conditions of Dirichlet or Neumann type:

$$h = \bar{h} \qquad \text{on } \partial_p \Omega, \qquad \mathbf{q} \cdot \mathbf{n} = \bar{q} \qquad \text{on } \partial_q \Omega \tag{11}$$

with $\partial_p \Omega \cup \partial_q \Omega = \partial \Omega$ and $\partial_p \Omega \cap \partial_q \Omega = \emptyset$, as well as the initial conditions

$$h = h^0 \qquad \text{for} \quad t = 0. \tag{12}$$

2.2. Solution for a simple setup

For the simple setup in Fig. 1a, the pressure head only depends on the vertical coordinate x_2 (assumed positive downward) and on the time t, hence we can write the head-based Richards equation as

$$C(h)\frac{\partial h}{\partial t} = \frac{d}{dx_2}\left[k(h)\left(\frac{dh}{dx_2} - 1\right)\right]. \tag{13}$$

The boundary and initial conditions read

$$\begin{array}{lllll} \text{initial conditions:} & h = h^0 & \text{for} & t = 0. & \\ \text{boundary conditions:} & h|_{x_2=0} = \bar{h}_0 & \text{or} & q|_{x_2=0} = \bar{q}_0, & \\ & h|_{x_2=H} = \bar{h}_H & \text{or} & q|_{x_2=H} = \bar{q}_H. & \end{array} \tag{14}$$

Table 1
Geometry and material parameters.

Property	Symbol	Value	Units
Height	H	0.05	m
water density	ρ_w	1000	kg/m^3
gravitational acceleration magnitude	g	10	m/s^2
Porosity	ϕ^0	0.41	–
Hydraulic conduct. (sat.)	k_L	$9.80 \cdot 10^{-9}$	m/s
Constant in v.G. relation	α_{vG}	0.028	m^{-1}
Constant in v.G. relation	n_{vG}	1.3	–
Constant in v.G. relation	S_r	0.15	–
Elastic modulus	E	1104	kPa
Poisson's ratio	ν	0.0	–
Bulk modulus	K	552	kPa
Critical stress	σ_c	7.06	kPa
Unit damage dissipation	w_1	0.045	kPa
Length-scale parameter	l	0.002 unless specified otherwise	m

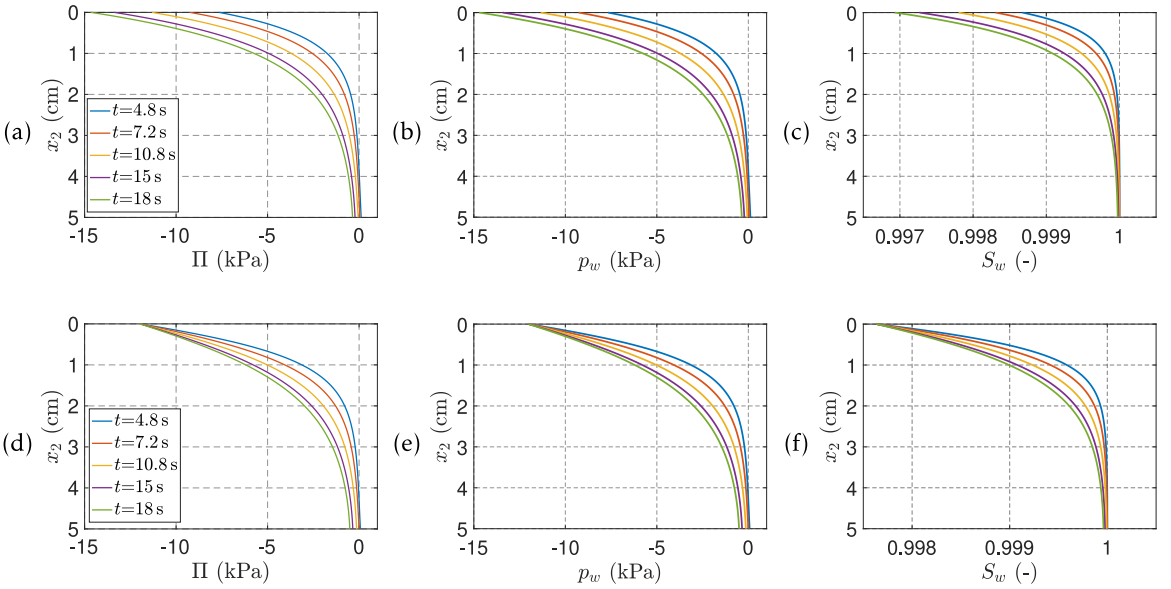

Fig. 2. Evolution of effective pore pressure, water pressure and saturation during (a–c) a flux-driven ($\bar{q}_0 = -6 \times 10^{-7}$ m/s) and (d–f) a pressure-driven ($\bar{h}_0 = -1.2$ m) drying process.

Moreover, the geometry and material parameters are listed in Table 1. With the given boundary and initial conditions, we solve the Richards equation with a finite difference scheme. After the pressure head profile $h(x_2)$ is derived at a given t, the effective pore pressure $\Pi(x_2) = \rho_w g h(x_2) S_w(h(x_2))$ is computed.

Fig. 2 illustrates the vertical distribution of effective pore pressure, water pressure and saturation at different time instances for a flux-driven and a pressure-driven case (in both cases, a zero flux boundary condition is applied on the bottom surface). In the flux-driven case with outward flux, as the water continuously flows out from the top (to represent in a simplified fashion the occurrence of evaporation), the water pressure reaches its minimum value there. The capillary pressure $p_c = -p_w$ is thus maximum on the top surface and decreases with increasing depth. According to the van Genuchten equation, the saturation is also lowest on the top. With time, the water pressure at any depth keeps decreasing and correspondingly, the soil becomes drier and drier until the residual saturation is reached (not shown). In the pressure-driven case, a constant capillary pressure is applied on the top. Under the pressure gradient, the water moves upwards such that the lower part of the domain becomes drier. This process stops when the pressure is homogeneous in the whole domain (not shown).

3. Variational damage problem

In this section, after introducing the free energy density of a variably saturated porous solid with no damage, we propose two general forms of the total energy density functional for the damaged case within the framework of variational phase-field models of brittle fracture [29,31,32]. Minimization yields the governing equations of the drying damage problem, namely the linear momentum balance equations for quasi-static problems and the damage evolution equation. We show that two models from the literature are special instances of the proposed general forms. By further specifying the two general forms, we propose two model families for variational phase-field modeling of drying damage.

3.1. Free energy density of a porous solid in the undamaged case

In this section, we consider a coupled hydro-mechanical setting to formulate the free energy density of a variably saturated porous solid in absence of damage. The related classical expression of the free energy will inspire the subsequent extended formulation of the total energy density for a variably saturated porous solid in presence of damage. Let us consider a body $\Omega \subset \mathbb{R}^d$ made of a variably saturated porous material whose current state is characterized by the vector-valued displacement field $\mathbf{u} : \mathbf{x} \in \mathbb{R}^d, t \in \mathbb{R}^+ \rightarrow \mathbf{u}(\mathbf{x}, t) \in \mathbb{R}^d$, and the effective pore pressure $\Pi : \mathbf{x} \in \mathbb{R}^d, t \in \mathbb{R}^+ \rightarrow \Pi(\mathbf{x}, t) \in \mathbb{R}$ defined as[2]

$$\Pi(\mathbf{x}, t) = S_w(\mathbf{x}, t) p_w(\mathbf{x}, t). \tag{15}$$

Assuming a geometrically linear model, the strain measure is the infinitesimal strain tensor,

$$\boldsymbol{\varepsilon}(\mathbf{u}, t) = \nabla^s \mathbf{u}, \tag{16}$$

with $\nabla^s(\bullet) = \frac{1}{2}\left[\nabla(\bullet) + \nabla^T(\bullet)\right]$ as the symmetric gradient operator. With a standard volumetric–deviatoric decomposition, we can write $\boldsymbol{\varepsilon} = \frac{1}{d}\epsilon \boldsymbol{I} + \boldsymbol{\varepsilon}_{\text{dev}}$, with $\epsilon = tr(\boldsymbol{\varepsilon})$ as the volumetric strain and $\boldsymbol{\varepsilon}_{\text{dev}}$ as the deviatoric strain tensor.

For this coupled poro-elastic problem, assuming incompressible solid grains (an assumption commonly made for soils) and no initial total stress, $\boldsymbol{\sigma}^0 = \mathbf{0}$, one can define the following free energy density functional[3] [54]

$$G(\boldsymbol{\varepsilon}, \Pi) = \psi(\boldsymbol{\varepsilon}) - \varphi(\boldsymbol{\varepsilon}, \Pi) \tag{17}$$

where

$$\psi(\boldsymbol{\varepsilon}) = \frac{1}{2}\boldsymbol{\varepsilon} \cdot \mathbb{C}\boldsymbol{\varepsilon} = \frac{1}{2}K\epsilon^2 + \mu \boldsymbol{\varepsilon}_{\text{dev}} \cdot \boldsymbol{\varepsilon}_{\text{dev}}, \qquad \varphi(\boldsymbol{\varepsilon}, \Pi) = \Pi\epsilon. \tag{18}$$

Here $\psi(\boldsymbol{\varepsilon})$ is the elastic strain energy density, with $\mathbb{C}$ as the fourth-order elasticity tensor, K as the bulk modulus and μ as the shear modulus,[4] and $\varphi(\boldsymbol{\varepsilon}, \Pi)$ can be interpreted as the mechanical work produced by the effective

[2] According to Dalton's law, the effective pore pressure can be defined by

$$\Pi = \sum_{\beta=1}^{n_\beta} S_\beta p_\beta,$$

where the sum is carried out over the n_β fluids in pores, e.g. water and air. Due to the passive air phase assumption recalled at the beginning of Section 2, this equation can be simplified as (15). Note that Coussy [54,55] proposes

$$\Pi = S_w p_w - U(S_w)$$

where $U(S_w) = -\int_{S_w}^1 p_w(S_w)\, dS_w$ is to be computed numerically using the inverse $p_w(S_w)$ of relationship (7). It can be shown that for our purposes, since first cracking occurs for values of saturation very close to 1, the values of $U(S_w)$ are very small and (15) suffices. In [57] it is also suggested to neglect the $U(S_w)$ term as its incorporation becomes very cumbersome in dynamics.

[3] In presence of initial strain $\boldsymbol{\varepsilon}^0$ (with volumetric component ϵ^0) and effective pore pressure Π^0, in this section the following substitutions should be made: $\boldsymbol{\varepsilon}$ with $\boldsymbol{\varepsilon} - \boldsymbol{\varepsilon}^0$, ϵ with $\epsilon - \epsilon^0$ and Π with $\Pi - \Pi^0$.

[4] For $d = 2$, the Lamé constants are related to Young's modulus E and Poisson's ratio ν as

$$\mu = \frac{E}{2(1+\nu)} \quad \text{and} \quad \lambda = \frac{E\nu}{1-\nu^2}$$

and the bulk modulus is given by $K = \lambda + \mu$.

pore pressure Π applied to the internal solid walls of the porous solid [55]. For the following discussion, we rewrite this equation in a different but equivalent form as follows

$$G\left(\boldsymbol{\varepsilon}_{\mathrm{e}}, \Pi\right) = \tilde{\psi}(\boldsymbol{\varepsilon}_{\mathrm{e}}) - \tilde{\varphi}(\Pi) \tag{19}$$

where the effective strain is introduced as

$$\boldsymbol{\varepsilon}_{\mathrm{e}} = \boldsymbol{\varepsilon} - \frac{\Pi}{dK}\mathbf{I}, \tag{20}$$

and

$$\tilde{\psi}(\boldsymbol{\varepsilon}_{\mathrm{e}}) = \frac{1}{2}\boldsymbol{\varepsilon}_{\mathrm{e}} \cdot \mathbb{C}\boldsymbol{\varepsilon}_{\mathrm{e}}, \qquad \tilde{\varphi}(\Pi) = \frac{1}{2}\frac{\Pi^2}{K}. \tag{21}$$

Note that although the first term $\tilde{\psi}$ has an analogous structure as ψ in (18), it depends not only on the solid strain but also on the effective pore pressure. Moreover, the second term $\tilde{\varphi}$ is now only dependent on the effective pore pressure.

3.2. Total energy density of a porous solid in the damaged case

In order to characterize the material state in a damage process, we introduce the irreversible scalar damage field $\alpha : \mathbf{x} \in \mathbb{R}^d, t \in \mathbb{R}^+ \rightarrow \alpha(\mathbf{x}, t) \in [0, 1]$, with the values 0 and 1 corresponding to an intact and a fully damaged material, respectively. Inspired by Eq. (17), a quite general expression of the total energy density functional for the damaged case can be proposed as

$$\mathcal{W}\left(\boldsymbol{\varepsilon}, \Pi, \alpha, \nabla\alpha\right) = A\left(\alpha\right)\psi^{+}\left(\boldsymbol{\varepsilon}\right) + \psi^{-}\left(\boldsymbol{\varepsilon}\right) - B\left(\alpha\right)\varphi^{+}(\boldsymbol{\varepsilon},\ \Pi) - \varphi^{-}(\boldsymbol{\varepsilon},\ \Pi) + w(\alpha) + \frac{1}{2}w_1 l^2 \nabla\alpha \cdot \nabla\alpha, \tag{22}$$

with $\psi = \psi^{+} + \psi^{-}$ and $\varphi = \varphi^{+} + \varphi^{-}$ according to some chosen decomposition (possible options will be specified later). This functional is composed of: the active and inactive parts of the solid strain energy density $\psi^{\pm}$, depending only on the solid strain; the active/inactive parts of the coupling energy density $\varphi^{\pm}$, depending on both the solid strain and the effective pore pressure, and the local and non-local damage dissipation terms depending on the damage (or phase-field) variable α and on its gradient $\nabla\alpha$. The local term is represented by the monotonically increasing function $w(\alpha)$ with $w(0) = 0$ and $w(1) = w_1 < \infty$, known as local damage dissipation function. The constant w_1 is the specific energy dissipation, representing the energy dissipated per unit volume to reach the fully damaged state from the pristine material during a homogeneous process. The non-local term depends on the gradient of the damage and contains an internal length scale parameter l.

The active parts of the energies are coupled with the phase-field variable by the degradation functions $A(\alpha)$ and $B(\alpha)$, for which possible simple choices read

$$A(\alpha) = (1-\alpha)^a, \quad B(\alpha) = (1-\alpha)^b \qquad a, b \in \mathbb{N}. \tag{23}$$

A general formulation of the total energy density functional alternative to (22), inspired by Eq. (19), may take the form

$$\tilde{\mathcal{W}}\left(\boldsymbol{\varepsilon}_{\mathrm{e}}, \Pi, \alpha, \nabla\alpha\right) = \tilde{A}\left(\alpha\right)\tilde{\psi}^{+}\left(\boldsymbol{\varepsilon}_{\mathrm{e}}\right) + \tilde{\psi}^{-}\left(\boldsymbol{\varepsilon}_{\mathrm{e}}\right) - \tilde{B}\left(\alpha\right)\tilde{\varphi}^{+}(\boldsymbol{\varepsilon}_{\mathrm{e}}, \Pi) - \tilde{\varphi}^{-}(\boldsymbol{\varepsilon}_{\mathrm{e}}, \Pi) + w(\alpha) + \frac{1}{2}w_1 l^2 \nabla\alpha \cdot \nabla\alpha. \tag{24}$$

Once again, $\tilde{\psi} = \tilde{\psi}^{+} + \tilde{\psi}^{-}$ and $\tilde{\varphi} = \tilde{\varphi}^{+} + \tilde{\varphi}^{-}$. Compared to Eq. (22), the key difference lies in the dependencies of the energy contributions on their arguments. Note that, although $\tilde{\varphi}$ only depends on Π, its active and inactive portions may depend on $\boldsymbol{\varepsilon}_{\mathrm{e}}$ if so does the decomposition. Analogous to the first form, the degradation functions may be chosen as

$$\tilde{A}(\alpha) = (1-\alpha)^{\tilde{a}}, \quad \tilde{B}(\alpha) = (1-\alpha)^{\tilde{b}} \qquad \tilde{a}, \tilde{b} \in \mathbb{N}. \tag{25}$$

Note that the above choices of the degradation functions trivially fulfill the requirements [31]:

$$A\left(0\right) = B\left(0\right) = \tilde{A}\left(0\right) = \tilde{B}\left(0\right) = 1, \quad A\left(1\right) = B\left(1\right) = \tilde{A}\left(1\right) = \tilde{B}\left(1\right) = 0, \tag{26}$$

$$A'\left(\alpha\right) < 0, \quad B'\left(\alpha\right) < 0, \quad \tilde{A}'\left(\alpha\right) < 0, \quad \tilde{B}'\left(\alpha\right) < 0. \tag{27}$$

For the damage dissipation function, we adopt

$$w(\alpha) = w_1 \alpha, \tag{28}$$

which yields a phase-field model of the AT1 type [58], characterized by an initially undamaged (elastic) response.

3.3. Uncoupled assumption and total energy

From now on, in order to enable the semi-analytical developments in the following sections, we uncouple the hydraulic problem (illustrated in Section 2) from the elastic problem with damage. In other words, we first compute the effective pore pressure by solving the Richards equation (5) with the van Genuchten equations (7), (8), and then consider this pressure as an input when solving for solid deformation and damage. Thus, the total energy density functionals in (22) and (24) are simplified as follows

$$\mathcal{W}(\boldsymbol{\varepsilon}, \alpha, \nabla\alpha; \Pi) = A(\alpha)\,\psi^+(\boldsymbol{\varepsilon}) + \psi^-(\boldsymbol{\varepsilon}) - B(\alpha)\,\varphi^+(\boldsymbol{\varepsilon}; \Pi) - \varphi^-(\boldsymbol{\varepsilon}; \Pi) + w(\alpha) + \frac{1}{2} w_1 l^2 \nabla\alpha \cdot \nabla\alpha, \tag{29}$$

$$\tilde{\mathcal{W}}(\boldsymbol{\varepsilon}_\mathrm{e}, \alpha, \nabla\alpha; \Pi) = \tilde{A}(\alpha)\,\tilde{\psi}^+(\boldsymbol{\varepsilon}_\mathrm{e}) + \tilde{\psi}^-(\boldsymbol{\varepsilon}_\mathrm{e}) - \tilde{B}(\alpha)\,\tilde{\varphi}^+(\boldsymbol{\varepsilon}_\mathrm{e}; \Pi) - \tilde{\varphi}^-(\boldsymbol{\varepsilon}_\mathrm{e}; \Pi) + w(\alpha) + \frac{1}{2} w_1 l^2 \nabla\alpha \cdot \nabla\alpha. \tag{30}$$

With a slight abuse of notation, we have kept the same symbols for the involved functionals and denoted with a semicolon the dependency on Π as a given (input) function rather than as an argument.

Finally, we define the total energy of the porous body in presence of damage as

$$\mathcal{E}(\mathbf{u}, \alpha; \Pi) = \int_\Omega \mathcal{W}(\boldsymbol{\varepsilon}(\mathbf{u}), \alpha, \nabla\alpha; \Pi)\, d\Omega \qquad \text{or} \qquad \tilde{\mathcal{E}}(\mathbf{u}, \alpha; \Pi) = \int_\Omega \tilde{\mathcal{W}}(\boldsymbol{\varepsilon}_\mathrm{e}(\mathbf{u}), \alpha, \nabla\alpha; \Pi)\, d\Omega \tag{31}$$

where, for simplicity, the contribution of external forces is neglected.

3.4. Evolution problem

Let the body Ω be subjected to the time-dependent pressure head $\bar{h}_t$ on $\partial_p\Omega$ or to the time-dependent water flux $\bar{q}_t$ on $\partial_q\Omega$. Within the uncoupled assumption, the solution of the hydraulic problem in Section 2 yields the pressure head field $h_t(\mathbf{x})$ and thus the water pore pressure field $p_{wt}(\mathbf{x})$, along with the saturation field $S_{wt}(\mathbf{x})$, resulting in the effective pore pressure field $\Pi_t(\mathbf{x})$ through (15). In the time-discrete version of variational gradient damage models, given the damage field α_p at the previous time-step t_p and a (small) time increment $\Delta t > 0$, the quasi-static equilibrium displacement $\mathbf{u}$ and the damage field α at the new time step $t = t_p + \Delta t$ are given by the solution of the energy minimization problem

$$(\mathbf{u}, \alpha) = \underset{(\hat{\mathbf{u}}, \hat{\alpha}) \in \mathcal{C}_t \times \mathcal{D}(\alpha_p)}{\text{arg loc min}}\, \mathcal{E}_t(\hat{\mathbf{u}}, \hat{\alpha}), \tag{32}$$

where

$$\mathcal{E}_t(\mathbf{u}, \alpha) = \mathcal{E}(\mathbf{u}, \alpha; \Pi_t) \tag{33}$$

and

$$\mathcal{C}_t := \{\mathbf{u} \in H^1(\Omega; \mathbb{R}^d) : \mathbf{u} = \bar{\mathbf{u}}_t \text{ on } \partial_D\Omega\}, \quad \mathcal{D}(\alpha_p) := \{\alpha \in H^1(\Omega; \mathbb{R}) : \alpha_p \le \alpha \le 1\}$$

are the spaces of the admissible displacement and damage fields at time t from the previous state with damage α_p. Here $H^1(\Omega; \mathbb{R}^d)$ denotes the usual Sobolev space of functions with square integrable first derivatives taking values in $\mathbb{R}^d$, and $\bar{\mathbf{u}}_t$ denotes the imposed displacement at time t on the Dirichlet boundary $\partial_D\Omega$ of the mechanical problem. In the energy minimization principle (32), *loc min* stands for local unilateral minimization, meaning that the solution $(\mathbf{u}, \alpha) \in \mathcal{C}_t \times \mathcal{D}(\alpha_p)$ should be such that

$$\forall (\hat{\mathbf{u}}, \hat{\alpha}) \in \mathcal{C}_t \times \mathcal{D}(\alpha_p),\ \exists \bar{m} > 0 :\ \forall m \in [0, \bar{m}] \quad \mathcal{E}_t(\mathbf{u} + m(\hat{\mathbf{u}} - \mathbf{u}), \alpha + m(\hat{\alpha} - \alpha)) - \mathcal{E}_t(\mathbf{u}, \alpha) \ge 0. \tag{34}$$

Retaining only the first-order series expansion of the energy increment in (34) gives the following variational inequality as a necessary condition for optimality:

$$\mathcal{E}_t'(\mathbf{u}, \alpha)(\hat{\mathbf{u}} - \mathbf{u}, \hat{\alpha} - \alpha) \ge 0, \quad \forall (\hat{\mathbf{u}}, \hat{\alpha}) \in \mathcal{C}_t \times \mathcal{D}(\alpha_p), \tag{35}$$

where

$$\mathcal{E}_t'(\mathbf{u},\alpha)(\mathbf{v},\beta) := \frac{d}{dm}\mathcal{E}_t(\mathbf{u}+m\mathbf{v},\alpha+m\beta)\Big|_{m=0}$$

denotes the directional derivative of the functional $\mathcal{E}_t(\mathbf{u},\alpha)$ in the direction $(\mathbf{v},\beta)$.

By suitably selecting the variations $\mathbf{v}$, β and applying standard localization arguments, one can show that, for smooth solutions, the first-order optimality condition (35) is equivalent to the following equilibrium equation and equilibrium boundary condition

$$\mathrm{div}\boldsymbol{\sigma}(\boldsymbol{\varepsilon},\alpha;\Pi_t)=\mathbf{0} \text{ on } \Omega, \quad \boldsymbol{\sigma}(\boldsymbol{\varepsilon},\alpha;\Pi_t)\mathbf{n}=\mathbf{0} \text{ on } \partial_N\Omega, \tag{36}$$

where $\partial_N\Omega$ is the Neumann boundary of the mechanical problem, and to the damage criterion

$$\alpha-\alpha_p\geq 0, \quad Y(\boldsymbol{\varepsilon},\alpha;\Pi_t)+\ell^2 w_1\Delta\alpha\leq 0, \quad (Y(\boldsymbol{\varepsilon},\alpha;\Pi_t)+\ell^2 w_1\Delta\alpha)(\alpha-\alpha_p)=0 \quad \text{on } \Omega, \tag{37a}$$

$$\alpha-\alpha_p\geq 0, \quad \nabla\alpha\cdot\mathbf{n}\geq 0, \quad (\nabla\alpha\cdot\mathbf{n})(\alpha-\alpha_p)=0 \quad \text{on } \partial\Omega, \tag{37b}$$

where $\mathbf{n}$ is the outer unit normal to the boundary $\partial\Omega$, $\Delta\alpha$ denotes the Laplacian of the damage field, and

$$\boldsymbol{\sigma}(\boldsymbol{\varepsilon},\alpha;\Pi_t) := \frac{\partial\mathcal{W}(\boldsymbol{\varepsilon},\alpha,\nabla\alpha;\Pi_t)}{\partial\boldsymbol{\varepsilon}} = A(\alpha)\frac{\partial\psi^+(\boldsymbol{\varepsilon})}{\partial\boldsymbol{\varepsilon}}+\frac{\partial\psi^-(\boldsymbol{\varepsilon})}{\partial\boldsymbol{\varepsilon}}-B(\alpha)\frac{\partial\varphi^+(\boldsymbol{\varepsilon};\Pi_t)}{\partial\boldsymbol{\varepsilon}}-\frac{\partial\varphi^-(\boldsymbol{\varepsilon};\Pi_t)}{\partial\boldsymbol{\varepsilon}} \tag{38a}$$

$$Y(\boldsymbol{\varepsilon},\alpha;\Pi_t) := -\frac{\partial\mathcal{W}(\boldsymbol{\varepsilon},\alpha,\nabla\alpha;\Pi_t)}{\partial\alpha} = -A'(\alpha)\psi^+(\boldsymbol{\varepsilon})+B'(\alpha)\varphi^+(\boldsymbol{\varepsilon};\Pi_t)-w'(\alpha) \tag{38b}$$

are the total Cauchy stress tensor and the damage energy release rate, respectively.

In a fully analogous fashion, we can derive the equilibrium equations, boundary conditions and damage criterion for the total energy $\tilde{\mathcal{E}}$, leading to

$$\mathrm{div}\boldsymbol{\sigma}(\boldsymbol{\varepsilon}_\mathrm{e},\alpha;\Pi_t)=\mathbf{0} \text{ on } \Omega, \quad \boldsymbol{\sigma}(\boldsymbol{\varepsilon}_\mathrm{e},\alpha;\Pi_t)\mathbf{n}=\mathbf{0} \text{ on } \partial_N\Omega, \tag{39}$$

and

$$\alpha-\alpha_p\geq 0, \quad Y(\boldsymbol{\varepsilon}_\mathrm{e},\alpha;\Pi_t)+\ell^2 w_1\Delta\alpha\leq 0, \quad (Y(\boldsymbol{\varepsilon}_\mathrm{e},\alpha;\Pi_t)+\ell^2 w_1\Delta\alpha)(\alpha-\alpha_p)=0 \quad \text{on } \Omega, \tag{40a}$$

$$\alpha-\alpha_p\geq 0, \quad \nabla\alpha\cdot\mathbf{n}\geq 0, \quad (\nabla\alpha\cdot\mathbf{n})(\alpha-\alpha_p)=0 \quad \text{on } \partial\Omega, \tag{40b}$$

where

$$\begin{aligned}\boldsymbol{\sigma}(\boldsymbol{\varepsilon}_\mathrm{e},\alpha;\Pi_t) &:= \frac{\partial\tilde{\mathcal{W}}(\boldsymbol{\varepsilon}_\mathrm{e},\alpha,\nabla\alpha;\Pi_t)}{\partial\boldsymbol{\varepsilon}_\mathrm{e}} \\ &= \tilde{A}(\alpha)\frac{\partial\tilde{\psi}^+(\boldsymbol{\varepsilon}_\mathrm{e};\Pi_t)}{\partial\boldsymbol{\varepsilon}_\mathrm{e}}+\frac{\partial\tilde{\psi}^-(\boldsymbol{\varepsilon}_\mathrm{e};\Pi_t)}{\partial\boldsymbol{\varepsilon}_\mathrm{e}}-\tilde{B}(\alpha)\frac{\partial\tilde{\varphi}^+(\boldsymbol{\varepsilon}_\mathrm{e};\Pi_t)}{\partial\boldsymbol{\varepsilon}_\mathrm{e}}-\frac{\partial\tilde{\varphi}^-(\boldsymbol{\varepsilon}_\mathrm{e};\Pi_t)}{\partial\boldsymbol{\varepsilon}_\mathrm{e}}\end{aligned} \tag{41a}$$

$$Y(\boldsymbol{\varepsilon}_\mathrm{e},\alpha;\Pi_t) := -\frac{\partial\tilde{\mathcal{W}}(\boldsymbol{\varepsilon}_\mathrm{e},\alpha,\nabla\alpha;\Pi_t)}{\partial\alpha} = -\tilde{A}'(\alpha)\tilde{\psi}^+(\boldsymbol{\varepsilon}_\mathrm{e};\Pi_t)+\tilde{B}'(\alpha)\tilde{\varphi}^+(\boldsymbol{\varepsilon}_\mathrm{e};\Pi_t)-w'(\alpha) \tag{41b}$$

(with a slight abuse of notation in using the same symbols for $\boldsymbol{\sigma}$ and Y in both cases). Equivalent conditions are obtained in a time-continuous setting as a consequence of an evolution principle based on irreversibility, energy balance, and stability, see [31,32,59] for further details.

3.5. Two model families

In the following section, we further specify the total energy forms of Section 3.3 and thus propose two model families for drying damage problems. Besides, we discuss the relation of the proposed families to models previously proposed in the literature. In this section, we focus on the volumetric–deviatoric split proposed in [35]. A discussion for the spectral decomposition is reported in Appendix.

3.5.1. Model family I, based on the decomposition of the strain

The first model family is based on Eq. (29), where the terms are specified as

$$\begin{aligned}&\psi^+(\boldsymbol{\varepsilon})=\mu\,\boldsymbol{\varepsilon}_\mathrm{dev}\cdot\boldsymbol{\varepsilon}_\mathrm{dev}+\frac{K}{2}\langle\epsilon\rangle_+^2, \quad \psi^-(\boldsymbol{\varepsilon})=\frac{K}{2}\langle\epsilon\rangle_-^2, \\ &\varphi^+(\epsilon;\Pi)=\Pi\langle\epsilon\rangle_+, \quad \varphi^-(\epsilon;\Pi)=\Pi\langle\epsilon\rangle_-.\end{aligned} \tag{42}$$

The total Cauchy stress tensor results as

$$\boldsymbol{\sigma} = \frac{\partial \mathcal{W}}{\partial \boldsymbol{\varepsilon}} = (1-\alpha)^a \left(2\mu \boldsymbol{\varepsilon}_{\text{dev}} + K \langle \epsilon \rangle_+ \mathbf{I}\right) + K \langle \epsilon \rangle_- \mathbf{I} - (1-\alpha)^b \, \Pi H(\epsilon)\mathbf{I} - \Pi H(-\epsilon)\mathbf{I}, \tag{43}$$

and the damage criterion reads

$$a\,(1-\alpha)^{a-1}\left(\mu\, \boldsymbol{\varepsilon}_{\text{dev}} \cdot \boldsymbol{\varepsilon}_{\text{dev}} + \frac{K}{2}\langle \epsilon \rangle_+^2\right) - b(1-\alpha)^{b-1}\Pi \langle \epsilon \rangle_+ - w_1 + w_1 l^2 \Delta\alpha \leq 0. \tag{44}$$

This model family couples the damage both to the solid elastic strain energy and to the effective pore pressure. The underlying idea is that the work of the capillary pressure (the negative of the water pore pressure) must decrease in presence of damage due to the loss of effectiveness in the capillary action. Correspondingly, damage degrades both the portion of the stress related to the solid strain (the so-called effective stress) and the portion related to the pore pressure, although possibly with a different degradation function, to account for the mechanical degradation of the solid skeleton and for the deterioration of the capillary action.

3.5.2. Model family II, based on the decomposition of the effective strain

The second model is based on Eq. (30). After noticing that the deviatoric parts of effective and solid strain are identical, we adopt the following choices

$$\begin{aligned} &\tilde{\psi}^+(\boldsymbol{\varepsilon}_{\text{e}};\, \Pi) = \mu\, \boldsymbol{\varepsilon}_{\text{dev}} \cdot \boldsymbol{\varepsilon}_{\text{dev}} + \frac{K}{2}\langle \epsilon_{\text{e}} \rangle_+^2, \quad && \tilde{\psi}^-(\boldsymbol{\varepsilon}_{\text{e}};\, \Pi) = \frac{K}{2}\langle \epsilon_{\text{e}} \rangle_-^2, \\ &\tilde{\varphi}^+(\epsilon_{\text{e}};\, \Pi) = H(\epsilon_{\text{e}})\frac{\Pi^2}{2K}, && \tilde{\varphi}^-(\epsilon_{\text{e}};\, \Pi) = H(-\epsilon_{\text{e}})\frac{\Pi^2}{2K}. \end{aligned} \tag{45}$$

where ϵ_{e} is the trace of the effective strain tensor. The resulting total Cauchy stress tensor is given by

$$\boldsymbol{\sigma} = \frac{\partial \tilde{\mathcal{W}}}{\partial \boldsymbol{\varepsilon}_{\text{e}}} = (1-\alpha)^{\tilde{a}}\left[K \langle \epsilon_{\text{e}} \rangle_+ \mathbf{I} + 2\mu \boldsymbol{\varepsilon}_{\text{dev}}\right] + K \langle \epsilon_{\text{e}} \rangle_- \mathbf{I}, \tag{46}$$

and the damage criterion reads

$$\tilde{a}\,(1-\alpha)^{\tilde{a}-1}\left[\mu \boldsymbol{\varepsilon}_{\text{dev}} \cdot \boldsymbol{\varepsilon}_{\text{dev}} + \frac{1}{2}K\langle \epsilon_{\text{e}} \rangle_+^2\right] - \tilde{b}(1-\alpha)^{\tilde{b}-1} H(\epsilon_{\text{e}})\frac{\Pi^2}{2K} - w_1 + w_1 l^2 \Delta\alpha \leq 0. \tag{47}$$

The idea of this model family is similar to that of the previous one; the only difference is that here the sign of the effective volumetric strain discriminates between active and inactive contributions of the total energy in relation to damage. In the following sections, this choice will be shown to have an important influence on the results.

3.5.3. Relation to existing models in the literature

In the work of Yoshioka and Bourdin [60], the total energy density reads[5]

$$\mathcal{W}(\boldsymbol{\varepsilon}, \alpha, \nabla\alpha;\, \Pi) = \frac{1}{2}\mathbb{C}\left((1-\alpha)\,\boldsymbol{\varepsilon} - \frac{\Pi}{3K}\mathbf{I}\right) \cdot \left((1-\alpha)\,\boldsymbol{\varepsilon} - \frac{\Pi}{3K}\mathbf{I}\right) - \frac{1}{2}\frac{\Pi^2}{K} \tag{48}$$

which can be reformulated as

$$\mathcal{W}(\boldsymbol{\varepsilon}, \alpha, \nabla\alpha;\, \Pi) = (1-\alpha)^2\left(\mu\, \boldsymbol{\varepsilon}_{\text{dev}} \cdot \boldsymbol{\varepsilon}_{\text{dev}} + \frac{K}{2}\epsilon^2\right) - (1-\alpha)\,\Pi\epsilon + w_1\alpha + \frac{1}{2}w_1 l^2 \nabla\alpha \cdot \nabla\alpha. \tag{49}$$

This model can be obtained from Eq. (29) with $a = 2$, $b = 1$ and

$$\begin{aligned} &\psi^+(\boldsymbol{\varepsilon}) = \mu\, \boldsymbol{\varepsilon}_{\text{dev}} \cdot \boldsymbol{\varepsilon}_{\text{dev}} + \frac{K}{2}\epsilon^2, \quad && \psi^-(\boldsymbol{\varepsilon}) = 0, \\ &\varphi^+(\epsilon,\, \Pi) = \Pi\epsilon, && \varphi^-(\epsilon,\, \Pi) = 0. \end{aligned} \tag{50}$$

The difference with respect to model family I is the absence of an energy decomposition. Note that the model was proposed for hydraulic fracture and not for drying fracture, which made such a decomposition unnecessary. The total Cauchy stress tensor is given by

$$\boldsymbol{\sigma} = \frac{\partial \mathcal{W}}{\partial \boldsymbol{\varepsilon}} = (1-\alpha)^2\,(2\mu\boldsymbol{\varepsilon} + \lambda\epsilon\mathbf{I}) - (1-\alpha)\,\Pi\mathbf{I} \tag{51}$$

[5] The original formulation does not contain the last term $\frac{1}{2}\frac{\Pi^2}{K}$; however, within the assumption of a given pressure field, this term has no influence on the expression of the stress — hence on the equilibrium equations — nor on the damage criterion.

and the damage criterion reads

$$2\,(1-\alpha)\left(\mu\,\boldsymbol{\varepsilon}\cdot\boldsymbol{\varepsilon}+\frac{\lambda}{2}\epsilon^2\right)-\Pi\epsilon-w_1+w_1 l^2\Delta\alpha\leq 0, \tag{52}$$

where both the solid strain and the effective pore pressure contribute to the crack evolution.

In the work of Cajuhi et al. [44], the following energy density[6] is adopted:

$$\mathcal{W}\left(\boldsymbol{\varepsilon},\alpha,\nabla\alpha;\Pi\right)=(1-\alpha)^2\left(\mu\,\boldsymbol{\varepsilon}_{\text{dev}}\cdot\boldsymbol{\varepsilon}_{\text{dev}}+\frac{K}{2}\langle\epsilon\rangle_+^2\right)+\frac{K}{2}\langle\epsilon\rangle_-^2-\Pi\epsilon+w_1\alpha+\frac{1}{2}w_1 l^2\nabla\alpha\cdot\nabla\alpha, \tag{53}$$

in which damage is only coupled to the solid deformation and not to the effective pore pressure. This is a special case of model family I with $a=2$ and $b=0$, The total Cauchy stress tensor takes the form

$$\boldsymbol{\sigma}=\frac{\partial\mathcal{W}}{\partial\boldsymbol{\varepsilon}}=(1-\alpha)^2\left(2\mu\boldsymbol{\varepsilon}_{\text{dev}}+K\langle\epsilon\rangle_+\mathbf{I}\right)+K\langle\epsilon\rangle_-\mathbf{I}-\Pi\mathbf{I} \tag{54}$$

and the damage criterion

$$2\,(1-\alpha)\left(\mu\,\boldsymbol{\varepsilon}_{\text{dev}}\cdot\boldsymbol{\varepsilon}_{\text{dev}}+\frac{K}{2}\langle\epsilon\rangle_+^2\right)-w_1+w_1 l^2\Delta\alpha\leq 0 \tag{55}$$

is independent of the effective pore pressure.

Finally, the model in [45] does not give an explicit expression of the energy density. The expression of the stress corresponds to that of model family II with $\tilde{a}=2$, however, the model in [45] being not variational, the damage criterion is not derived from the same energy as the stress.

4. Evaluation of the phase-field model families I and II

In this section, for the desiccation process modeled in Section 2, we use the setups in Figs. 1b,c to examine the performance of the variational damage model families introduced in Section 3 for two types of boundary conditions, namely free and restrained desiccation. As observed in experimental tests on clayey soils [16,61,62], we expect no damage in the first case and damage in the second case.

Throughout the analysis, to avoid through-thickness effects, we assume $d=2$. The first evaluation of the performance of the models is based on the computation of the effective pore pressure leading to the first occurrence of damage. In pristine conditions, the damage variable and its derivatives are zero in the whole domain. According to the Kuhn–Tucker conditions in Section 3.4, damage evolution starts when

$$\begin{aligned}&-A'(0)\,\psi^+\left(\boldsymbol{\varepsilon}\left(\Pi_c\right)\right)+B'(0)\,\varphi^+\left(\boldsymbol{\varepsilon}\left(\Pi_c\right);\Pi_c\right)-w_1=0\\&-\tilde{A}'(0)\,\tilde{\psi}^+\left(\boldsymbol{\varepsilon}_{\text{e}}\left(\Pi_c\right);\Pi_c\right)+\tilde{B}'(0)\,\tilde{\varphi}^+\left(\boldsymbol{\varepsilon}_{\text{e}}\left(\Pi_c\right);\Pi_c\right)-w_1=0\end{aligned} \tag{56}$$

for model families I and II, respectively. We have denoted with Π_c the effective pore pressure at first damage (named as critical effective pore pressure from now on). Subsequently, other considerations are made on the damage mode.

4.1. Free desiccation test

For the setup in Fig. 1b, assuming the hydraulic problem in Fig. 1a has been solved on the same domain as shown in Section 2, we now solve the elasticity problem in absence of damage and compute the value of the effective pore pressure for which the first damage occurs.

4.1.1. Elasticity problem

For the setup in Fig. 1b, in which the porous material is free to deform, the boundary conditions read

$$\begin{aligned}&u_1|_{x_1=0}=u_2|_{x_2=H}=0,\quad \sigma_{12}|_{x_1=0}=\sigma_{12}|_{x_2=H}=0\\&\boldsymbol{\sigma}\cdot\mathbf{n}|_{x_1=L}=\boldsymbol{\sigma}\cdot\mathbf{n}|_{x_2=0}=\mathbf{0}.\end{aligned} \tag{57}$$

Thus, we immediately obtain

$$\sigma_{11}\left(x_2\right)=\sigma_{22}\left(x_2\right)=0,\quad \sigma_{11}^{\text{eff}}\left(x_2\right)=\sigma_{22}^{\text{eff}}\left(x_2\right)=\Pi\left(x_2\right)<0, \tag{58}$$

[6] The original formulation is fully coupled, i.e. the effective pore pressure field is not considered as an input, but solved along with the displacement and the damage fields.

where $\boldsymbol{\sigma}^{\text{eff}}(\mathbf{x}, t)$ is the effective stress tensor, with $\boldsymbol{\sigma} = \boldsymbol{\sigma}^{\text{eff}} - \Pi\mathbf{I}$. This relationship is derived from the generalized effective stress principle for variably saturated soils proposed by Schrefler [63], see also [64,65], combined with the passive air phase assumption [53]. During the drying process the sign of the effective pore pressure is negative as per the results in Section 2; in the case of free drying this leads to negative effective stress components, i.e. to compression of the solid skeleton. From the effective stresses we can compute the horizontal and vertical strains (principal strains) as

$$\varepsilon_{11}(x_2) = \frac{1}{E}\left(\sigma_{11}^{\text{eff}}(x_2) - \nu\sigma_{22}^{\text{eff}}(x_2)\right) = \varepsilon_{22}(x_2) = \frac{1-\nu}{E}\Pi(x_2) < 0 \tag{59}$$

where E and ν are the Young's modulus and the Poisson's ratio, respectively, and the volumetric strain

$$\epsilon(x_2) = \frac{2(1-\nu)}{E}\Pi(x_2) = \frac{\Pi(x_2)}{K} < 0. \tag{60}$$

Thus the (purely volumetric) strain tensor corresponds to isotropic shrinkage.

4.1.2. Effective pore pressure at first damage

Based on the solution of the elasticity problem, it is straightforward to check from (58) that no value of effective pore pressure can ever lead to damage for any of the proposed model families. Hence, all models are able to reproduce the absence of damage for the free desiccation case.

4.2. Constrained desiccation test

We now repeat the previous analysis for the setup in Fig. 1c, where the horizontal deformation is prevented.

4.2.1. Elasticity problem

For the setup in Fig. 1c the boundary conditions are:

$$\begin{aligned} &u_1|_{x_1=0} = u_1|_{x_1=L} = u_2|_{x_2=H} = 0 \\ &\sigma_{12}|_{x_1=0} = \sigma_{12}|_{x_1=L} = \sigma_{12}|_{x_2=H} = 0 \\ &\boldsymbol{\sigma}\cdot\mathbf{n}|_{x_2=0} = \mathbf{0}. \end{aligned} \tag{61}$$

The equilibrium equation in the vertical direction and the compatibility in the horizontal direction yield

$$\frac{d\sigma_{22}(x_2)}{dx_2} = 0 \quad \text{and} \quad \varepsilon_{11}(x_2) = 0. \tag{62}$$

Due to the Neumann boundary conditions for $x_2 = 0$, it is then

$$\sigma_{22}(x_2) = 0 = \sigma_{22}^{\text{eff}}(x_2) - \Pi(x_2). \tag{63}$$

From the stress–strain relationship follows

$$\varepsilon_{22}(x_2) = \frac{\Pi(x_2)}{\lambda + 2\mu} < 0 \tag{64}$$

and hence we can write the strain tensor and its deviatoric part,

$$\boldsymbol{\varepsilon}(x_2) = \begin{bmatrix} 0 & 0 \\ 0 & \varepsilon_{22}(x_2) \end{bmatrix}, \quad \boldsymbol{\varepsilon}_{\text{dev}}(x_2) = \begin{bmatrix} -\frac{1}{2}\varepsilon_{22}(x_2) & 0 \\ 0 & \frac{1}{2}\varepsilon_{22}(x_2) \end{bmatrix}, \tag{65}$$

as well as the volumetric strain and volumetric effective strain

$$\epsilon(x_2) = \varepsilon_{22}(x_2) = \frac{\sigma_{22}^{\text{eff}}(x_2)}{\lambda + 2\mu} = \frac{\Pi(x_2)}{\lambda + 2\mu} < 0, \quad \epsilon_{\text{e}}(x_2) = \frac{-\mu\Pi(x_2)}{(\lambda + 2\mu)(\lambda + \mu)} > 0. \tag{66}$$

Table 2
Summary of the response of model families I and II.

Model family	Π_c		Crack mode
	Free desiccation	Restrained desiccation	
I	–	$-(2\mu+\lambda)\sqrt{\frac{2w_1}{a\mu}}$	II
II	–	$-\sqrt{\frac{2(2\mu+\lambda)(\mu+\lambda)w_1}{\mu(\tilde{a}-2\tilde{b})+\lambda\tilde{b}}}$, $\tilde{a} > \frac{2}{1-\nu}\tilde{b}$	I/II

4.2.2. Effective pore pressure at first damage

For model family I, it is straightforward to determine the critical effective pore pressure such that $(56)_1$ is satisfied as

$$\Pi_c = -(\lambda+2\mu)\sqrt{\frac{2w_1}{a\mu}}, \tag{67}$$

so the model is able to predict damage initiation for a sufficiently large effective pore pressure regardless of the choice of the parameters a (which influences Π_c) and b (which plays no role for Π_c). Note that $a = 2$ corresponds to the model of Cajuhi et al. [44].

For model family II, the critical effective pore pressure is easily obtained as

$$\Pi_c = -\sqrt{\frac{2(\lambda+2\mu)(\lambda+\mu)w_1}{\mu(\tilde{a}-2\tilde{b})+\lambda\tilde{b}}} \tag{68}$$

and has a real value if

$$\tilde{a} > \frac{2}{1-\nu}\tilde{b}. \tag{69}$$

It is immediate to check that the model in Yoshioka and Bourdin [60] cannot predict crack initiation under the given setup (which it was not intended for).

4.2.3. Damage mode

As shown in Eq. (66), in the restrained desiccation case, the volumetric strain is negative whereas the volumetric effective strain is positive. This implies that for model family I damage is driven purely by the deviatoric strain energy, whereas model family II predicts damage driven by a combination of volumetric and deviatoric strain energies. This aspect is relevant for the comparison to experimental results, which seem to indicate a predominance of mode-I cracking or combined mode-I/II. Hence, at least qualitatively, the comparison is more favorable with model family II.

4.2.4. Summary

Table 2 provides a summary of the results obtained in this section. The following observations can be drawn:

- For the free desiccation setup, the model families I and II result in no damage evolution, which is consistent with the experimental evidence.
- For the restrained desiccation setup, both model families result in damage evolution for an effective pore pressure exceeding (in absolute value) a critical effective pore pressure Π_c, which is again consistent with the experimental evidence. The existence of a real value of Π_c poses restrictions on the choice of the coefficients $\tilde{a}$ and $\tilde{b}$ in model family II, whereas it holds irrespective of the choice of a and b (natural numbers) in model family I.
- Damage initiation results from the pure deviatoric strain energy for model family I, and from a combination of volumetric and deviatoric strain energies for model family II. This suggests that model family II better relates to the experimental evidence of mode-I or combined mode-I/II cracking [8,15].

Based on the above assessment, we choose model family II for the subsequent analysis.

5. Homogeneous damage and onset of localization in restrained desiccation

In this section, we concentrate on model family II with $\tilde{a} = 2$ and $\tilde{b} = 0$. At each time, the effective pore pressure field is computed upfront by solving the hydraulic problem as shown in Section 2.2. For the restrained desiccation setup, along the lines of [51] for the restrained thermal problem, we first seek a fundamental solution with homogeneous damage (i.e. damage invariant with respect to the x_1 coordinate, parallel to the surface of the slab). Then we look for the bifurcated solution, which represents the onset of the localization phenomena leading to the periodic crack pattern observed in the experiments.

5.1. Homogeneous solution for damage evolution

As follows, we seek a fundamental solution with homogeneous damage (i.e. damage invariant with respect to x_1). We first formulate the related one-dimensional boundary value problem, and then solve it numerically.

5.1.1. Theoretical formulation

In the solution of the Richards equation for the desiccation problem, the boundary conditions are applied as illustrated in Section 2.2 prescribing a negative water pressure or an outflux on the top surface. For both cases, at a given instant of time, the capillary pressure and the absolute value of the effective pore pressure decrease gradually along the depth of the slab. Hence, the minimum (or maximum in absolute value) effective pore pressure is reached on the top surface and we denote it as $\Pi_{0t} = \Pi_t(x_2 = 0)$. For later use, we introduce the dimensionless variables

$$F_t(x_2) = \frac{\Pi_t(x_2)}{\Pi_{0t}}, \quad \theta = \frac{\Pi_c}{\Pi_{0t}} \tag{70}$$

with $F_t(x_2) \leq 1.0$. θ measures the ratio between the critical effective pore pressure and the minimum one, which reflects the mildness of the drying phenomenon. The lower θ, the more intense is the drying. Note that θ is a function of time, θ_t, in flux-driven desiccation and is a constant, $\bar{\theta}$, in pressure-driven desiccation. If $|\Pi_{0t}| < |\Pi_c|$, or $\theta > 1$, the critical effective pore pressure is not reached anywhere in the slab, hence the elastic solution in Section 4.2.1 is valid and no damage occurs. This happens in flux-driven desiccation at early instants of time, or in pressure-driven desiccation at all times if $\bar{\theta} > 1$. However, if $|\Pi_{0t}| > |\Pi_c|$, or $\theta < 1$, it can be easily seen that the damage criterion is violated within a region $0 < x_2 < \hat{x}_t$. Looking at the time evolution of $\Pi_t(x_2)$ in Fig. 2, it is also evident that $\hat{x}_t$ grows over time, so that it is reasonable to assume damage to occur within this region. Since the effective pore pressure only depends on x_2 and t, we also expect a damage field $\alpha_t(x_2)$.

Inserting this form into (62) and (61), we immediately find out that the displacement and strain fields in the damaged case are the same as in the elastic solution,

$$\boldsymbol{\varepsilon}_t(x_2) = \begin{bmatrix} 0 & 0 \\ 0 & \varepsilon_{22t}(x_2) \end{bmatrix}, \quad \boldsymbol{\varepsilon}_{\mathrm{dev}t}(x_2) = \begin{bmatrix} -\frac{1}{2}\varepsilon_{22t}(x_2) & 0 \\ 0 & \frac{1}{2}\varepsilon_{22t}(x_2) \end{bmatrix}, \tag{71}$$

with

$$\varepsilon_{22t}(x_2) = \frac{\Pi_t(x_2)}{\lambda + 2\mu} < 0, \tag{72}$$

whereas the total stress tensor field becomes

$$\boldsymbol{\sigma}_t(x_2) = [1 - \alpha_t(x_2)]^2 \left[K\epsilon_{et}(x_2)\mathbf{I} + 2\mu\boldsymbol{\varepsilon}_{\mathrm{dev}t}(x_2)\right]. \tag{73}$$

In order to find $\alpha_t(x_2)$, we note that the damage criterion (47) with $\tilde{a} = 2$ and $\tilde{b} = 0$ reads

$$[1 - \alpha_t(x_2)]\frac{\mu\Pi_t^2(x_2)}{(\lambda + 2\mu)(\lambda + \mu)} - w_1 + w_1 l^2 \alpha_t''(x_2) \leq 0 \tag{74}$$

which, using Eq. (68), can be rewritten as[7]

$$[1 - \alpha_t(x_2)]F_t^2(x_2) - \theta^2 + \theta^2 l^2 \alpha_t''(x_2) \leq 0 \tag{75}$$

[7] It is straightforward to show that Eq. (75) is also valid for model family I, provided that Eq. (67) is used to compute Π_c.

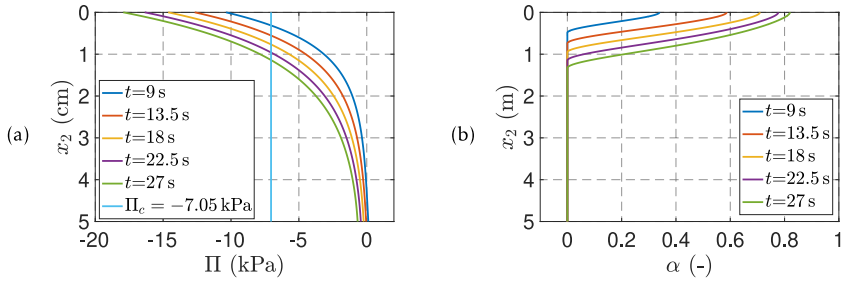

Fig. 3. Evolution of (a) effective pore pressure Π and (b) damage variable α for the flux-driven case.

Assuming that damage is only non-zero for $0 \leq x_2 < \hat{x}_t$, where $\hat{x}_t$ is still unknown, we conclude that $\alpha_t\,(x_2)$ must satisfy the differential equation

$$[1 - \alpha_t\,(x_2)]F_t^2\,(x_2) - \theta^2 + \theta^2 l^2 \alpha_t''\,(x_2) = 0, \quad 0 \leq x_2 \leq \hat{x}_t, \tag{76}$$

with boundary conditions

$$\alpha_t'\,(0) = 0, \qquad \alpha_t\left(\hat{x}_t\right) = 0, \qquad \alpha_t'\left(\hat{x}_t\right) = 0. \tag{77}$$

5.1.2. Numerical results

As follows, we provide numerical results for the homogeneous damage evolution in both flux-driven and pressure-driven desiccation. The hydraulic problem is the same as in Section 2.2 and all geometry and material parameters are given in Table 1. The critical effective pore pressure computed by Eq. (68) reads $\Pi_c = -7.05$ kPa.

We start with the flux-driven case, adopting an outflux of 6×10^{-7} m/s as in [44,45,66], leading to the time evolution of the effective pore pressure in Fig. 3a. When the effective pore pressure at the top exceeds the critical value Π_c, the damage variable starts to evolve. To compute the damage variable, we then use at each time instant a shooting method, which solves numerically the initial value problem represented by Eq. (76) with boundary conditions $(77)_{2,3}$ and searches for the value of $\hat{x}_t$ that satisfies $(77)_1$. Fig. 3b illustrates the damage profiles corresponding to the pressure profiles at selected time instants. All curves show that the damage variable decreases with the depth. The damage depth $\hat{x}_t$ increases with time while the magnitude of the damage variable α_t at any given depth also grows, thus automatically satisfying irreversibility of damage evolution which is not explicitly enforced.

Now we consider the pressure-driven case with $\bar{\theta} < 1$, where three constant pressure heads, i.e. $\bar{h}_0 = -1.2$ m, -1.8 m or -10 m, are applied on the top boundary. The corresponding drying mildness ratios, according to Eq. (70), are $\bar{\theta} = 0.59, 0.39, 0.09$. Moreover, five different length-scale parameters ranging from 1×10^{-3} m to 1×10^{-5} m are tested for each $\bar{\theta}$, see Fig. 4. Also in this case, the damage variable always decreases with the depth. Comparing the curves corresponding to a given length-scale parameter and different $\bar{\theta}$, we conclude that for more intense drying (lower $\bar{\theta}$), the maximum damage variable at the top is larger, and the damage depth is also larger. Comparing curves obtained for the same pressure head and different length-scale parameters, we notice that the damage field converges towards a limit one as l approaches zero. From Eq. (75) for $l \to 0$, we obtain that

$$\alpha_t\,(x_2 = 0) \to 1 - \bar{\theta}^2 \;\text{ and }\; \Pi(\hat{x}) \to \Pi_c \;\text{ for }\; l \to 0. \tag{78}$$

5.2. Bifurcation

Along the lines of Sicsic et al. [52], we now investigate the stability of the solution with homogeneous damage obtained in Section 5.1. The objective is to find out whether and when the solution can bifurcate from the fundamental branch (homogeneous damage) to another branch (localized damage).

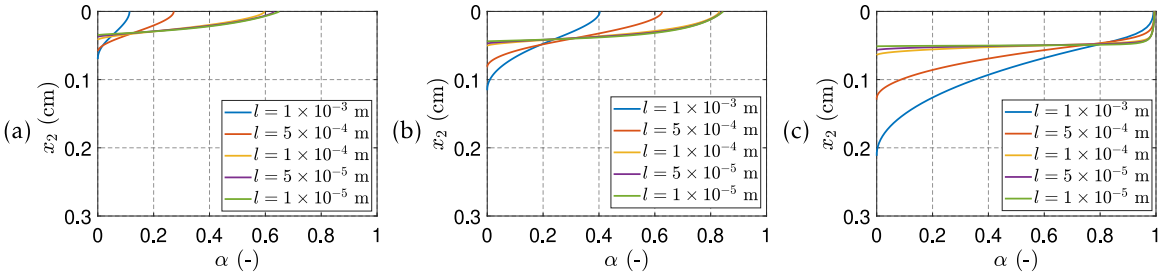

Fig. 4. Damage profile in the depth direction at $t = 1 \times 10^{-4}$ s for three pressure-driven cases: (a) $\bar{\theta} = 0.59$ ($\bar{h}_0 = -1.2$ m), (b) $\bar{\theta} = 0.39$ ($\bar{h}_0 = -1.8$ m), and (c) $\bar{\theta} = 0.09$ ($\bar{h}_0 = -10$ m).

5.2.1. Theoretical formulation

In order to evaluate the stability of the solution, we consider the second directional derivative of the energy functional of Eq. (31)$_2$ at $(\mathbf{u}_t,\, \alpha_t)$ in the direction $(\mathbf{v},\, \beta)$ as

$$\begin{aligned}\mathcal{E}_t''(\mathbf{u}_t,\, \alpha_t)(\mathbf{v},\, \beta) = \int_\Omega \Bigg\{ &\left[\tilde{A}\,(\alpha_t)\,\frac{\partial^2}{\partial \boldsymbol{\varepsilon}^2}\tilde{\psi}^+\,(\boldsymbol{\varepsilon}_\mathrm{e}\,(\mathbf{u}_t)) + \frac{\partial^2}{\partial \boldsymbol{\varepsilon}^2}\tilde{\psi}^-\,(\boldsymbol{\varepsilon}_\mathrm{e}\,(\mathbf{u}_t))\right] \cdot (\boldsymbol{\varepsilon}\,(\mathbf{v}) \otimes \boldsymbol{\varepsilon}\,(\mathbf{v})) \\ &+ 2\tilde{A}'\,(\alpha_t)\,\frac{\partial}{\partial \boldsymbol{\varepsilon}}\tilde{\psi}^+\,(\boldsymbol{\varepsilon}_\mathrm{e}\,(\mathbf{u}_t)) \cdot \boldsymbol{\varepsilon}\,(\mathbf{v})\,\beta \\ &+ \left[\tilde{A}''\,(\alpha_t)\,\tilde{\psi}^+\,(\boldsymbol{\varepsilon}_\mathrm{e}\,(\mathbf{u}_t)) - B''\,(\alpha_t)\,\varphi^+\,(\boldsymbol{\varepsilon}_\mathrm{e}\,(\mathbf{u}_t))\right]\beta^2 + w_1 l^2 \nabla\beta \cdot \nabla\beta \Bigg\}\, d\Omega.\end{aligned} \tag{79}$$

For the model in Section 3.5.2 with $\tilde{a} = 2$, $\tilde{b} = 0$, we specifically obtain

$$\begin{aligned}\mathcal{E}_t''(\mathbf{u}_t,\, \alpha_t)(\mathbf{v},\, \beta) = \int_\Omega \big\{ &(1-\alpha_t)^2\, 2\mu \boldsymbol{\varepsilon}_\mathrm{dev}\,(\mathbf{v}) \cdot \boldsymbol{\varepsilon}_\mathrm{dev}\,(\mathbf{v}) + (1-\alpha_t)^2 H(\epsilon_\mathrm{e}\,(\mathbf{u}_t)) K \epsilon^2(\mathbf{v}) \\ &+ H(-\epsilon_\mathrm{e}\,(\mathbf{u}_t)) K \epsilon^2(\mathbf{v}) - 8(1-\alpha_t)\,\mu \boldsymbol{\varepsilon}_\mathrm{dev}\,(\mathbf{u}_t) \cdot \boldsymbol{\varepsilon}_\mathrm{dev}\,(\mathbf{v})\,\beta \\ &- 4\,(1-\alpha_t)\,K\,\langle \epsilon_\mathrm{e}\,(\mathbf{u}_t)\rangle_+\,\epsilon\,(\mathbf{v})\,\beta \\ &+ 2\mu \boldsymbol{\varepsilon}_\mathrm{dev}\,(\mathbf{u}_t) \cdot \boldsymbol{\varepsilon}_\mathrm{dev}\,(\mathbf{u}_t)\,\beta^2 + K\,\langle \epsilon_\mathrm{e}\,(\mathbf{u}_t)\rangle_+^2\,\beta^2 + w_1 l^2 \nabla\beta \cdot \nabla\beta \,\}\, d\Omega.\end{aligned} \tag{80}$$

The solution obtained from Eqs. (39) and (40) is stable if the second directional derivative satisfies

$$\mathcal{E}_t''(\mathbf{u}_t,\, \alpha_t)(\hat{\mathbf{u}} - \mathbf{u}_t,\, \hat{\alpha} - \alpha_t) > 0, \quad \forall (\hat{\mathbf{u}}, \hat{\alpha}) \in \mathcal{C}_t \times \mathcal{D}(\alpha_p). \tag{81}$$

Next, we adopt for the variations $\mathbf{v} = \hat{\mathbf{u}} - \mathbf{u}_t$ and $\beta = \hat{\alpha} - \alpha_t$ the ansatz

$$\begin{aligned}&\mathbf{v} = \frac{\Pi_t\, \hat{x}_t}{2\,(\mu + \lambda)}\left[V_1^k\,(x_2)\,\sin\left(\omega^k x_1\right)\mathbf{e}_1 + V_2^k\,(x_2)\,\cos\left(\omega^k x_1\right)\mathbf{e}_2\right], \\ &\beta = B^k\,(x_2)\,\cos\left(\omega^k x_1\right),\end{aligned} \tag{82}$$

where $\omega^k = \dfrac{k\pi}{L}$, k is a natural number denoting the number of waves within the length L, and V_1^k, V_2^k, B^k are dimensionless coefficients. The ansatz for $\mathbf{v}$ automatically satisfies the boundary conditions

$$v_1|_{x=0,L} = 0, \qquad \left.\frac{\partial v_2}{\partial x_1}\right|_{x_1=0,L} = 0, \tag{83}$$

whereas the ansatz for β fulfills the Neumann boundary condition in Eq. (40), i.e.

$$\left.\frac{\partial \beta}{\partial x_1}\right|_{x_1=0,L} = 0. \tag{84}$$

According to the definition of the damage depth, $\hat{x}_t$, we also take

$$\beta = 0 \quad \text{for } x_2 > \hat{x}_t. \tag{85}$$

We now introduce the following dimensionless variables

$$\xi = \frac{x_2}{\hat{x}_t}, \quad \kappa = \omega^k\, \hat{x}_t, \quad \tau = \frac{\hat{x}_t}{l}, \tag{86}$$

which are all time-dependent through the damage depth. Thus, the second directional derivative in (80) can be rewritten as

$$\mathcal{E}_t''(\mathbf{V}^\kappa,\ B^\kappa) = (2\mu+\lambda)\frac{L}{2}\frac{\omega^k}{\theta^2}\hat{x}_t\mathcal{S}^\kappa(\mathbf{V}^\kappa,\ B^\kappa), \tag{87}$$

where

$$\mathcal{S}^\kappa = \mathcal{S}^\kappa_{0\to 1} + \mathcal{S}^\kappa_{1\to H/\hat{x}_t} \tag{88}$$

with

$$\begin{aligned}\mathcal{S}^\kappa_{0\to 1} = \int_0^1 \frac{(1-\alpha_\tau)^2}{1-\nu^2}\left[\kappa^2 V_1^{\kappa 2} + V_2^{\kappa\prime 2} + 2\nu\kappa V_1^\kappa V_2^{\kappa\prime} + \frac{1}{2}(1-\nu)\left(V_1^{\kappa\prime} - \kappa V_2^\kappa\right)^2\right] \\ + 4(1-\alpha_\tau)\kappa F_\tau V_1^\kappa B^\kappa + \left[F_\tau^2 + \left(\frac{\theta\kappa}{\tau}\right)^2\right]B^{\kappa 2} + \left(\frac{\theta}{\tau}\right)^2 B^{\kappa\prime 2}\mathrm{d}\xi \\ \mathcal{S}^\kappa_{1\to H/\hat{x}_t} = \int_1^{H/\hat{x}_t} \frac{1}{1-\nu^2}\left[\kappa^2 V_1^{\kappa 2} + V_2^{\kappa\prime 2} + 2\nu\kappa V_1^\kappa V_2^{\kappa\prime} + \frac{1}{2}(1-\nu)\left(V_1^{\kappa\prime} - \kappa V_2^\kappa\right)^2\right]\mathrm{d}\xi.\end{aligned} \tag{89}$$

From (87) it is clear that the positiveness of the second directional derivative is equivalent to that of $\mathcal{S}^\kappa$. Here we proceed as in Sicsic et al. [52] and study the positiveness of $\mathcal{S}^\kappa$ by comparing with zero the smallest eigenvalue of the corresponding discrete quadratic form. To this end, we first compute the second integral in (89), and, assuming the damage depth to be much smaller than the height of the sample, we approximate it as follows

$$\mathcal{S}^\kappa_{1\to H/\hat{x}_t} \approx \mathcal{S}^\kappa_{1\to\infty} = \int_1^\infty \frac{1}{1-\nu^2}\left[\kappa^2 V_1^{\kappa 2} + V_2^{\kappa\prime 2} + 2\nu\kappa V_1^\kappa V_2^{\kappa\prime} + \frac{1}{2}(1-\nu)\left(V_1^{\kappa\prime} - \kappa V_2^\kappa\right)^2\right]\mathrm{d}\xi. \tag{90}$$

We then minimize this integral over all $\mathbf{V}^\kappa$ of sufficient regularity by solving the Euler–Lagrange equations

$$\begin{cases} (\omega^k)^2 V_1^\kappa + \omega^k\nu V_2^{\kappa\prime} - \frac{1}{2}(1-\nu)(V_1^{\kappa\prime\prime} - \omega^k V_2^{\kappa\prime}) = 0 \\ -\omega^k\nu V_1^{\kappa\prime} - V_2^{\kappa\prime\prime} - \frac{1}{2}\left(\omega^k V_1^{\kappa\prime} - (\omega^k)^2 V_2^{\kappa\prime}\right) = 0 \end{cases} \tag{91}$$

with boundary conditions

$$V_1^\kappa(1) = A, \quad V_2^\kappa(1) = C, \quad V_1^\kappa(\infty) = V_1^{\kappa\prime}(\infty) = V_2^\kappa(\infty) = V_2^{\kappa\prime}(\infty) = 0. \tag{92}$$

Using the following ansatz functions

$$V_1^\kappa = A\mathrm{e}^{-\kappa(\xi-1)} + B\kappa(\xi-1)\mathrm{e}^{-\kappa(\xi-1)}, \quad V_2^\kappa = C\mathrm{e}^{-\kappa(\xi-1)} + D\kappa(\xi-1)\mathrm{e}^{-\kappa(\xi-1)}, \tag{93}$$

from (91), we obtain

$$B = D = \frac{1+\nu}{3-\nu}(C-A), \tag{94}$$

which leads to

$$V_1^\kappa = \left[A + \frac{1+\nu}{3-\nu}(C-A)\omega(\xi-1)\right]\mathrm{e}^{-\omega(\xi-1)}, \quad V_2^\kappa = \left[C + \frac{1+\nu}{3-\nu}(C-A)\omega(\xi-1)\right]\mathrm{e}^{-\omega(\xi-1)}. \tag{95}$$

Thus,

$$\min_{\mathbf{V}^\kappa\in H^1(1,\infty)^2}\mathcal{S}^\kappa_{1\to\infty} = \frac{2\kappa}{(1+\nu)(3-\nu)}\left[V_1^{\kappa 2}(1) + (1-\nu)V_1^\kappa(1)V_2^\kappa(1) + V_2^{\kappa 2}(1)\right], \tag{96}$$

and our next objective is to investigate the positive definiteness of

$$\begin{aligned}\bar{\mathcal{S}}^\kappa = \int_0^1 \left\{\frac{(1-\alpha_\tau)^2}{1-\nu^2}\left[\kappa^2 V_1^{\kappa 2} + V_2^{\kappa\prime 2} + 2\nu\kappa V_1^\kappa V_2^{\kappa\prime} + \frac{1}{2}(1-\nu)\left(V_1^{\kappa\prime} - \kappa V_2^\kappa\right)^2\right]\right. \\ \left. + 4(1-\alpha_\tau)\kappa F_\tau V_1^\kappa B^\kappa + \left[F^2 + \left(\frac{\theta\kappa}{\tau}\right)^2\right]B^{\kappa 2} + \left(\frac{\theta}{\tau}\right)^2 B^{\kappa\prime 2}\right\}\mathrm{d}\xi \\ + \frac{2\kappa}{(1+\nu)(3-\nu)}\left[V_1^{\kappa 2}(1) + (1-\nu)V_1^\kappa(1)V_2^\kappa(1) + V_2^{\kappa 2}(1)\right].\end{aligned} \tag{97}$$

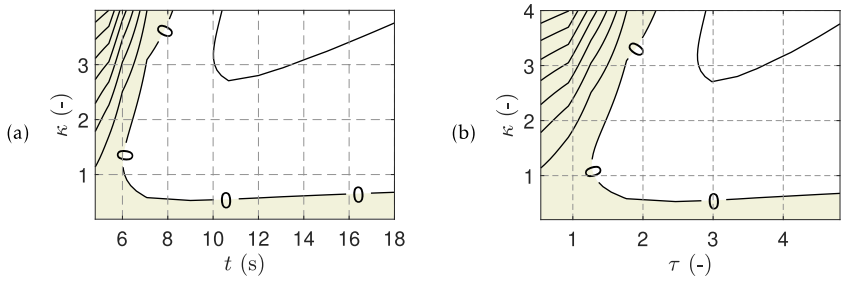

Fig. 5. Contour of the minimal eigenvalue μ_1 for a flux-driven case, $\bar{q} = 6 \times 10^{-7}$ m/s (the yellow area is for a stable solution where $\mu_1 > 0$).

The fundamental branch is stable if the quadratic form $\bar{\mathcal{S}}^{\kappa}$ is positive definite for any $\kappa \in \mathbb{R}^+$. Computationally, we can assess stability by computing the sign of the minimum eigenvalue of the matrix associated to the spatially discrete counterpart of $\bar{\mathcal{S}}^{\kappa}$. Hence, we discretize V_1^{κ}, V_2^{κ} and B^{κ} with linear shape functions and a uniform mesh for $\xi \in [0, 1]$, express the discrete quadratic form as

$$\bar{\mathcal{S}}_h^{\kappa} = \boldsymbol{\mathcal{V}} \cdot (\mathbf{K}^{\kappa} \boldsymbol{\mathcal{V}}) \,, \tag{98}$$

where $\boldsymbol{\mathcal{V}}$ is the vector of the nodal degrees of freedom, and seek the smallest eigenvalue of the matrix $\mathbf{K}^{\kappa}$ at a given τ and κ,

$$\mu_1(\tau, \kappa) = \min \operatorname{eig} (\mathbf{K}^{\kappa}) \,. \tag{99}$$

If $\mu_1 > 0$ for any $\kappa \in \mathbb{R}^+$, the fundamental solution is stable and no bifurcation occurs. Otherwise, the positiveness of the second directional derivative of the energy is not guaranteed and bifurcation may take place.

5.2.2. Numerical results

With the effective pore pressure and the damage variable derived in the last numerical examples, we can construct $\mathbf{K}^{\kappa}$ for a given κ and compute its minimum eigenvalue μ_1. Under either flux-driven or pressure-driven boundary conditions for increasing time, we can use the bisection algorithm to find the smallest τ such that $\mu_1 = 0$ for a fixed κ. By repeating the calculation for varying κ, the critical curve $\mu_1(\tau, \kappa) = 0$ is determined.

We first consider the flux-driven case in Section 5.1.2, for which the distribution of the effective pore pressure and the fundamental (homogeneous) solution for the damage variable are shown in Fig. 3. We compute μ_1 for $t \in [5, 18]$ s and $\kappa \in [0.2, 4.0]$, and draw the contour plots for $\mu_1(t, \kappa)$ and $\mu_1(\tau, \kappa)$ in Fig. 5. These figures show the critical curve $\mu_1(t, \kappa) = 0$ or $\mu_1(\tau, \kappa) = 0$; the shaded area is characterized by a positive minimum eigenvalue μ_1. These contours also reveal that approximately when $t < 6$ s, or $\tau < 1.2$, μ_1 is positive for any κ, thus, the homogeneous solution is stable. The earliest time where μ_1 becomes negative is $t_b = 6$ s ($\tau_b = 1.2$) and the corresponding value of κ is $\kappa_b = 1.26$. It should be mentioned that the above time is the moment when a bifurcated solution becomes possible. However, the homogeneous solution may still hold, hence, bifurcation does not necessarily occur at this moment.

For a pressure-driven case we obtain analogous contours, see Fig. 6. For a mild drying intensity $\bar{\theta} = 0.59$ ($\bar{h}_0 = -1.2$ m), the bifurcation time t_b is around 0.7 s and the corresponding scaled time τ_b and scaled frequency κ_b are both around 1.2. The evolution of μ_1 as a function of τ for different values of κ is given in Fig. 7. The minimum eigenvalue at a given κ is positive for small τ and decreases with time. A larger κ corresponds to a larger initial μ_1, but also to a higher rate of decrease.

In Fig. 8 we plot $\tau(\kappa)$ as obtained from the critical curve $\mu_1(\kappa, \tau) = 0$ for five different values of the drying mildness ratio $\bar{\theta}$. The minimum of each curve has coordinates κ_b, τ_b corresponding to the given $\bar{\theta}$. These coordinates are plotted in Fig. 9 as functions of θ. The behavior of τ_b is non-monotonic (Fig. 9a), whereas the corresponding frequency κ_b monotonically increases (i.e. the spacing of the initial cracks decreases) as the drying intensity increases ($\bar{\theta}$ decreases), see Fig. 9b.

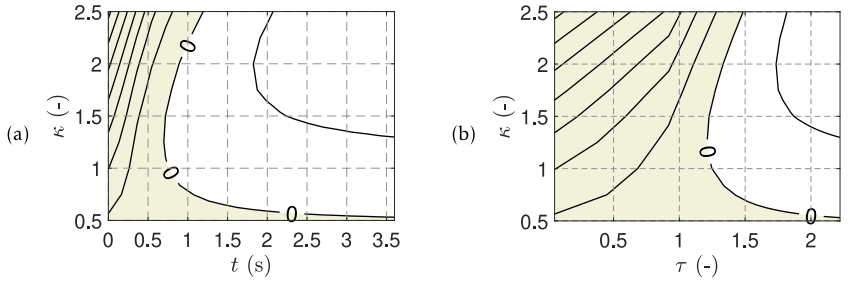

Fig. 6. Contour of the minimal eigenvalue μ_1 for a pressure-driven case, $\bar{\theta} = 0.59$ ($\bar{h} = -1.2$ m) (yellow area is for a stable solution where $\mu_1 > 0$).

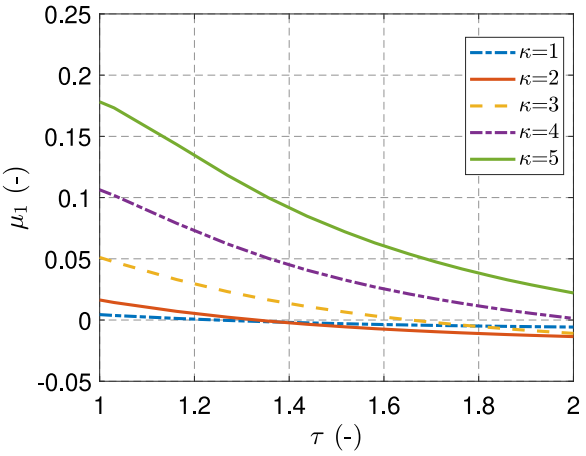

Fig. 7. Evolution of the minimal eigenvalue μ_1 for different values of the scaled frequency κ in the pressure-driven case with $\bar{\theta} = 0.59$ ($\bar{h} = -1.2$ m).

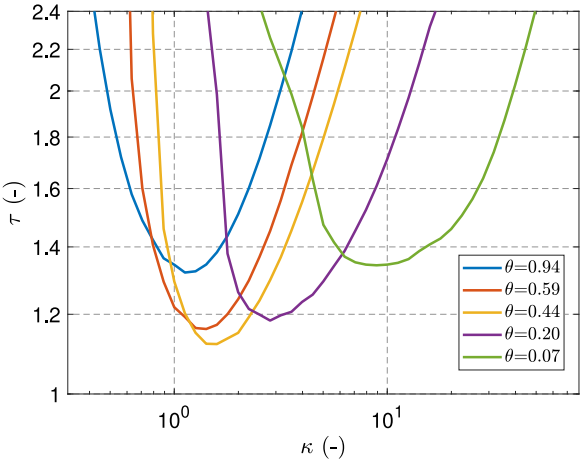

Fig. 8. Critical bifurcation curves in pressure-driven cases with different values of the drying mildness ratio $\bar{\theta}$.

5.2.3. Finite element simulation results

Finally, we compare the one-dimensional numerical results for the pressure-driven case with two-dimensional finite element simulations. The geometry and material parameters are those of Section 5.1.2, see Fig. 1(a, c) and Table 1. A constant water pressure, $\bar{h}_0 = -0.8$ m, is applied to the top boundary and the remaining hydraulic

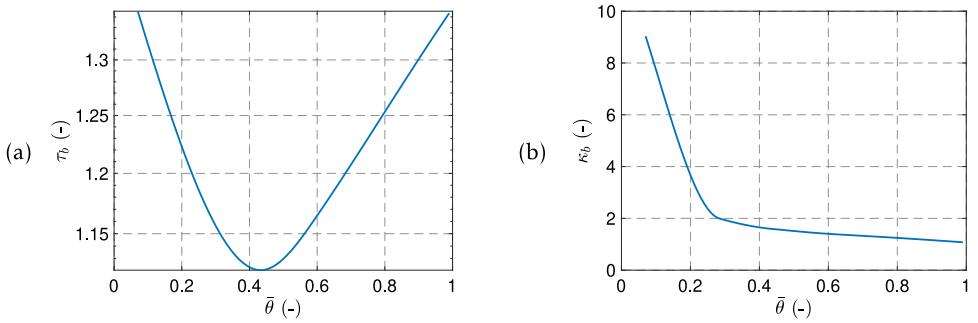

Fig. 9. Dimensionless bifurcation time and corresponding frequency as functions of $\bar{\theta}$ in pressure-driven cases.

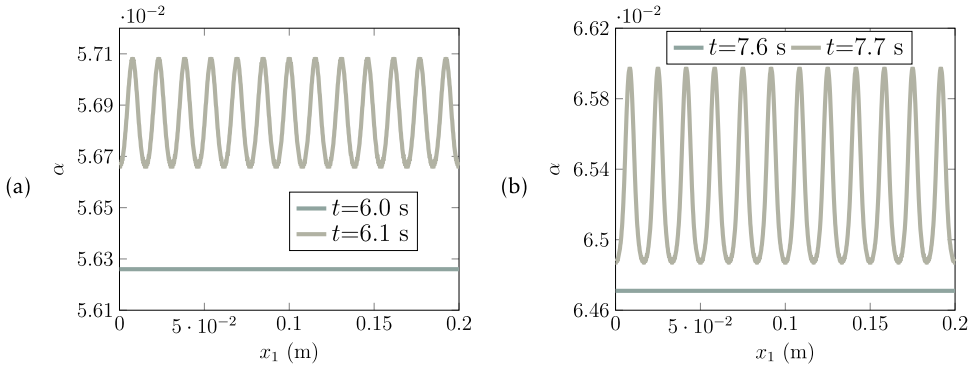

Fig. 10. Damage variable along the top boundary before/after the first bifurcation time for a pressure-driven case, $\bar{h} = -0.8$ m. (a) $\text{TOL}_{\text{ST}} = 10^{-10}$, (b) $\text{TOL}_{\text{ST}} = 10^{-9}$.

boundary conditions are as in Fig. 1(a). At each time step ($\Delta t = 0.1$ s), we first compute the water pressure by solving the hydraulic problem, then we solve the mechanical equations for the displacement field and the damage variable using a staggered solution scheme, which is stopped when a tolerance $\text{TOL}_{\text{ST}} = 10^{-10}$ is met on the residual norm. Within the staggered scheme, each of the two sub-problems (solving for the displacement or the damage) is iteratively solved with the Newton–Raphson method, using a tolerance $\text{TOL}_{\text{NR}} = 10^{-11}$ on the residual norm. To enforce irreversibility of the damage variable, we use the penalty method as proposed in [67].

The first bifurcated solution is found at time 6.1 s, see Fig. 10a, and the corresponding wave number is 12. When plotting the corresponding point on the contour of $\mu_1(\tau, \kappa)$ in Fig. 11, we find the point to be exactly located on the critical line determined in the previous section. Interestingly, if TOL_{ST} is lowered to 10^{-9} (a value much lower than those typically adopted in the literature [48,67]), we obtain the blue point, thus we overestimate τ_b and underestimate κ_b. This high sensitivity of the estimate of the bifurcation point to the tolerance of the staggered scheme is probably due to the very small values of the damage variable variation at bifurcation, as evident from Fig. 10, as well as to the fact that instability in critical conditions may but does not necessarily have to occur.

With $\text{TOL}_{\text{ST}} = 10^{-10}$, we also carry out the finite element computations for the flux-driven case in Section 5.2.2. The time increment is 0.025 s, and the first bifurcated solution is found at 5.65 s. The damage variable field features thirteen waves along the top boundary, see Fig. 12a. Also in this case, the corresponding point (τ, κ) is located on the critical line $\mu_1 = 0$ in the contour of the minimal eigenvalue, see Fig. 12b.

6. Conclusions

Phase-field modeling has already proved to be a suitable framework to predict the initiation and propagation of drying cracks in variably saturated porous media. In this paper, we focused on fundamental modeling aspects which had not yet been given sufficient attention: i. the influence of different choices for the coupling between the damage and the poro-mechanical fields and for the energy decomposition on the capability of a variational phase-field model

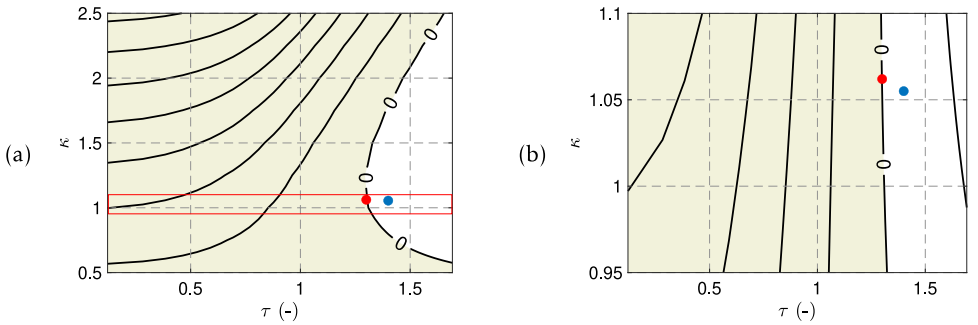

Fig. 11. Contour of the minimal eigenvalue μ_1 for the pressure-driven case, $\bar{h} = -0.8$ m. The shaded area denotes a stable fundamental solution as $\mu_1 > 0$. The red point corresponds to the finite element prediction with $\text{TOL}_{\text{ST}} = 10^{-10}$, whereas the blue point is obtained for $\text{TOL}_{\text{ST}} = 10^{-9}$. (For interpretation of the references to color in this figure legend, the reader is referred to the web version of this article.)

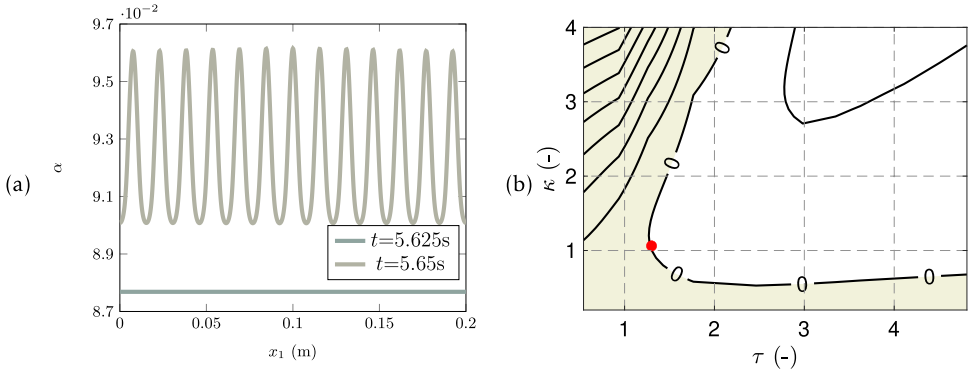

Fig. 12. (a) Damage variable along the top boundary before/after the first bifurcation time for a flux-driven case $\bar{q} = 6 \times 10^{-7}$m/s (b) Contour of the minimal eigenvalue μ_1 for the flux-driven case. The shaded area denotes a stable fundamental solution as $\mu_1 > 0$. The red point corresponds to the finite element prediction with $\text{TOL}_{\text{ST}} = 10^{-10}$. (For interpretation of the references to color in this figure legend, the reader is referred to the web version of this article.)

to realistically describe desiccation cracking, at least qualitatively; ii. the prediction of nucleation of a periodic array of cracks as a result of the loss of stability of a fundamental solution with homogeneous damage distribution.

In the first part of the paper, we summarized possible formulations for the total energy, characterized by different coupling and energy decomposition choices, into two model families, each with two free parameters. We then evaluated these families based on their ability to lead to qualitatively reasonable predictions for two benchmark cases, i.e. free and restrained desiccation. We found out that family II, based on coupling of the damage field with the total stress and on an energy decomposition related to the sign of the effective strain, leads to qualitatively reasonable predictions for both benchmark cases, as well as to damage initiation under mixed-mode conditions.

In the second part of the paper, we extended the analysis of Sicsic et al. [52], valid for thermal shock problems, to restrained desiccation under a given capillary pressure distribution, resulting from the solution of Richards equation with either flux-driven or pressure-driven boundary conditions. Through the variational analysis of the quasi-static damage evolution, we showed that this evolution follows first a fundamental branch without localization, and then bifurcates into another branch with damage localization, which leads to the initiation of a periodic array of cracks. The analysis enables the computation of the instant of time leading to crack initiation, as well of the corresponding crack spacing, as functions of geometry, material and (hydraulic) loading parameters. These results were found to be in excellent agreement with those of finite element simulations, provided that a sufficiently low tolerance is adopted for convergence of the alternate minimization scheme (much lower than typical tolerances adopted in the current literature).

Future research will concentrate on the fully coupled version of the proposed phase-field modeling approach and on the numerical solution of the related desiccation problem, as well as on the comparison with available

experimental results, towards the ultimate goal of *quantitatively* predicting desiccation cracking in partially saturated porous media. Another interesting research direction would be the determination of the parameters of the (inherently macroscopic) phase-field model based on the consideration of the complex phenomena taking place at lower observational scales.

Declaration of competing interest

The authors declare that they have no known competing financial interests or personal relationships that could have appeared to influence the work reported in this paper.

Data availability

Data will be made available on request.

Appendix. Discussion about the spectral decomposition

Here, we discuss the model families I and II with the spectral decomposition for the two cases in Section 4. With this decomposition, the active and inactive strain energies are defined as [36]

$$\psi^+ = \mu \langle \gamma_i \rangle_+^2 + \frac{1}{2}\lambda \langle \epsilon \rangle_+^2, \quad \psi^- = \mu \langle \gamma_i \rangle_-^2 + \frac{1}{2}\lambda \langle \epsilon \rangle_-^2. \tag{100}$$

where γ_i are the eigenvalues of the strain tensor $\boldsymbol{\varepsilon}$. Analogous to Eq. (42), we propose the total energy density functional for model family I as

$$\begin{aligned}\mathcal{W}(\boldsymbol{\varepsilon}, \alpha, \nabla\alpha; \Pi) = (1-\alpha)^a \left(\mu \langle \gamma_i \rangle_+^2 + \frac{1}{2}\lambda \langle \epsilon \rangle_+^2\right) + \mu \langle \gamma_i \rangle_-^2 + \frac{1}{2}\lambda \langle \epsilon \rangle_-^2 - (1-\alpha)^b \Pi \langle \epsilon \rangle_+ - \Pi \langle \epsilon \rangle_- \\ + w_1\alpha + \frac{1}{2}w_1 l^2 \nabla\alpha \cdot \nabla\alpha.\end{aligned} \tag{101}$$

According to the definition of the effective strain in Eq. (20), we further propose the functional of model family II as

$$\begin{aligned}\tilde{\mathcal{W}}(\boldsymbol{\varepsilon}_\mathrm{e}, \alpha, \nabla\alpha; \Pi) = (1-\alpha)^a \left(\mu \langle \gamma_i^\mathrm{e} \rangle_+^2 + \frac{1}{2}\lambda \langle \epsilon_\mathrm{e} \rangle_+^2\right) + \mu \langle \gamma_i^\mathrm{e} \rangle_-^2 + \frac{1}{2}\lambda \langle \epsilon_\mathrm{e} \rangle_-^2 \\ - (1-\alpha)^{\tilde{b}} \left[H(\epsilon_\mathrm{e})\frac{\Pi^2}{2K}\right] - H(-\epsilon_\mathrm{e})\frac{\Pi^2}{2K} + w_1\alpha + \frac{1}{2}w_1 l^2 \nabla\alpha \cdot \nabla\alpha.\end{aligned} \tag{102}$$

where γ_i^e are the eigenvalues of the effective strain tensor. For the free desiccation case in Section 4.1.1, the eigenvalues of the solid strain and the effective strain are

$$\gamma_1 = \gamma_2 = \frac{\Pi}{2K} < 0, \gamma_1^\mathrm{t} = \gamma_2^\mathrm{t} = 0. \tag{103}$$

Thus, for both model families, the material stays indefinitely elastic because the corresponding active energies are always zero. For constrained desiccation in Section 4.2.1, there exists no critical effective pore pressure for model family I, being

$$\psi^+(\boldsymbol{\varepsilon}) = 0, \quad \varphi^+(\boldsymbol{\varepsilon}, \Pi) = 0. \tag{104}$$

Thus, model family I based on the spectral decomposition is unable to simulate drying cracks under restrained boundary conditions. For model family II, we first derive the principal effective strains as

$$\gamma_1^\mathrm{e}(x_2) = \frac{\lambda \Pi(x_2)}{2(\lambda+\mu)(\lambda+2\mu)} < 0, \quad \gamma_2^\mathrm{e}(x_2) = -\frac{\Pi(x_2)}{2(\lambda+\mu)} > 0 \tag{105}$$

and the corresponding crack criterion is then given by

$$(\tilde{a}\frac{\mu(\lambda^2+6\lambda\mu+4\mu^2)}{4(\lambda+\mu)^2(\lambda+2\mu)^2} - \tilde{b}\frac{1}{2K})\Pi_c^2 - w_1 = 0. \tag{106}$$

The critical effective pore pressure is real if

$$\tilde{a} > \frac{2(\lambda+\mu)(\lambda+2\mu)^2}{\mu(\lambda^2+6\lambda\mu+4\mu^2)}\tilde{b} = \frac{2(1+\nu)}{\nu^3-2\nu^2+1}\tilde{b}. \tag{107}$$

E.g. for $\tilde{a}=2$ and $\tilde{b}=0$, the critical effective pore pressure is computed as

$$\tilde{\Pi}_c = -(1-\nu)\sqrt{\frac{w_1 E(1+\nu)}{(-\nu^2+\nu+1)}}. \tag{108}$$

References

[1] H. Peron, T. Hueckel, L. Laloui, L. Hu, Fundamentals of desiccation cracking of fine-grained soils: Experimental characterisation and mechanisms identification, Can. Geotech. J. 46 (10) (2009) 1177–1201.
[2] D. Brutin, B. Sobac, B. Loquet, J. Sampol, Pattern formation in drying drops of blood, J. Fluid Mech. 667 (2011) 85–95.
[3] J. Hubert, A. Léonard, E. Plougonven, F. Collin, Resorcinol formaldehyde hydrogel drying behavior: Desiccation cracking modeling, in: Proceedings of the 7th European Drying Conference, 2019, pp. 68–75.
[4] S. Tarafdar, T. Dutta, Formation of desiccation crack patterns in electric fields: A review, Phil. Trans. R. Soc. A 377 (2136) (2019) 20170398.
[5] C.-S. Tang, C. Zhu, Q. Cheng, H. Zeng, J.-J. Xu, B.-G. Tian, B. Shi, Desiccation cracking of soils: A review of investigation approaches, underlying mechanisms, and influencing factors, Earth Sci. Rev. (2021) 103586.
[6] H. Péron, L. Hu, L. Laloui, T. Hueckel, Numerical and experimental investigation of desiccation of soil, in: Proceedings of the 3rd Asian Conference on Unsaturated Soils, International Society for Soil Mechanics and Geotechnical Engineering, 2007, pp. 391–396.
[7] R.A. Stirling, Multiphase Modelling of Desiccation Cracking in Compacted Soil (Ph.D. thesis), Newcastle University, 2014.
[8] X. Wei, M. Hattab, P. Bompard, J.-M. Fleureau, Highlighting some mechanisms of crack formation and propagation in clays on drying path, Géotechnique 66 (4) (2016) 287–300.
[9] N. Mohammad, W. Meng, Y. Zhang, M. Liu, A. El-Zein, Y. Gan, Desiccation crack formation and prevention in thin bentonite layers, Environ. Geotech. 40 (2020) 1–15.
[10] S. Costa, J. Kodikara, N.I. Thusyanthan, Modelling of desiccation crack development in clay soils, in: Proc. 12th International Conference of IACMAG, Goa, India, 2008, pp. 1099–1107.
[11] R.A. Stirling, P.N. Hughes, C.T. Davie, S. Glendinning, Cyclic relationship between saturation and tensile strength in the near-surface zone of infrastructure embankments, in: Sixth International Conference on Unsaturdated Soils, UNSAT 2014, Newcastle University, 2014, pp. 1501–1505.
[12] R.A. Stirling, D.G. Toll, S. Glendinning, P.R. Helm, A. Yildiz, P.N. Hughes, J.D. Asquith, Weather-driven deterioration processes affecting the performance of embankment slopes, Géotechnique (2020) 1–13.
[13] L.-L. Wang, C.-S. Tang, B. Shi, Y.-J. Cui, G.-Q. Zhang, I. Hilary, Nucleation and propagation mechanisms of soil desiccation cracks, Eng. Geol. 238 (2018) 27–35.
[14] X. Wei, L. Ighil Ameur, F.J. -M., P. Bompard, M. Hattab, Highlighting some mechanisms of crack formation of clay mixture under free desiccation, in: Proc. the SEC 2015 International Symposium, 2015, pp. 1–10.
[15] A.E. Hajjar, T. Ouahbi, I. Hamrouni, S. Taibi, J. Eid, M. Hattab, Experimental characterization of desiccation cracking mechanisms in clayey soils, Eur. J. Environ. Civ. Eng. (2022) http://dx.doi.org/10.1080/19648189.2022.2136249.
[16] H. Péron, Desiccation Cracking of Soils (Ph.D. thesis), École Polytechnique Fédérale de Lausanne, Lausanne, Switzerland, 2009.
[17] C.-S. Tang, B. Shi, C. Liu, L. Gao, H.I. Inyang, Experimental investigation of the desiccation cracking behavior of soil layers during drying, J. Mater. Civ. Eng. 23 (6) (2011) 873–878.
[18] L. Goehring, S.W. Morris, Cracking mud, freezing dirt, and breaking rocks, Phys. Today 67 (2014) 39.
[19] A.L. Amarasiri, J.K. Kodikara, S. Costa, Numerical modelling of desiccation cracking, Int. J. Numer. Anal. Methods Geomech. 35 (1) (2011) 82–96.
[20] L. Hu, H. Péron, T. Hueckel, L. Laloui, Numerical and phenomenological study of desiccation of soil, in: Advances in Unsaturated Soil, Seepage, and Environmental Geotechnics, American Society of Civil Engineers, 2006, pp. 166–173.
[21] R. Rodríguez, M. Sanchez, A. Ledesma, A. Lloret, Experimental and numerical analysis of desiccation of a mining waste, Can. Geotech. J. 44 (6) (2007) 644–658.
[22] D. Asahina, J.E. Houseworth, J.T. Birkholzer, J. Rutqvist, J.E. Bolander, Hydro-mechanical model for wetting/drying and fracture development in geomaterials, Comput. Geosci. 65 (2014) 13–23.
[23] R.A. Stirling, C.T. Davie, S. Glendinning, Multiphase modelling of desiccation cracking in the near-surface of compacted soils, in: Geotechnical Engineering for Infrastructure and Development, 2015, pp. 2311–2316, http://dx.doi.org/10.1680/ecsmge.60678.vol4.353.
[24] R.A. Stirling, S. Glendinning, C.T. Davie, Modelling the deterioration of the near surface caused by drying induced cracking, Appl. Clay Sci. 146 (2017) 176–185.
[25] T.D. Vo, A. Pouya, S. Hemmati, A.M. Tang, Numerical modelling of desiccation cracking of clayey soil using a cohesive fracture method, Comput. Geotech. 85 (2017) 15–27.
[26] A. Pouya, T.D. Vo, S. Hemmati, A.M. Tang, Modeling soil desiccation cracking by analytical and numerical approaches, Int. J. Numer. Anal. Methods Geomech. 43 (3) (2019) 738–763.
[27] T.D. Vo, A. Pouya, S. Hemmati, A.M. Tang, Modelling desiccation crack geometry evolution in clayey soils by analytical and numerical approaches, Can. Geotech. J. 56 (5) (2019) 720–729.

[28] D.K. Tran, N. Ralaizafisoloarivony, R. Charlier, B. Mercatoris, A. Léonard, D. Toye, A. Degré, Studying the effect of desiccation cracking on the evaporation process of a luvisol—from a small-scale experimental and numerical approach, Soil Tillage Res. 193 (2019) 142–152.
[29] B. Bourdin, G. Francfort, J.-J. Marigo, Numerical experiments in revisited brittle fracture, J. Mech. Phys. Solids 48 (4) (2000) 797–826.
[30] G.A. Francfort, J.-J. Marigo, Revisiting brittle fracture as an energy minimization problem, J. Mech. Phys. Solids 46 (8) (1998) 1319–1342.
[31] K. Pham, J.-J. Marigo, The variational approach to damage: I. The foundations [Approche variationnelle de l'endommagement: I. Les concepts fondamentaux], C. R. Mec. 338 (4) (2010) 191–198.
[32] K. Pham, J.-J. Marigo, The variational approach to damage: II. The gradient damage models, Acad. Sci. C. R. Mec. 338 (4) (2010) 199–206.
[33] M. Ambati, T. Gerasimov, L. De Lorenzis, A review on phase-field models of brittle fracture and a new fast hybrid formulation, Comput. Mech. 55 (2) (2015) 383–405.
[34] M.F. Wheeler, T. Wick, S. Lee, IPACS: Integrated phase-field advanced crack propagation simulator. An adaptive, parallel, physics-based-discretization phase-field framework for fracture propagation in porous media, Comput. Methods Appl. Mech. Engrg. 367 (2020) 113124.
[35] H. Amor, J.-J. Marigo, C. Maurini, Regularized formulation of the variational brittle fracture with unilateral contact: Numerical experiments, J. Mech. Phys. Solids 57 (8) (2009) 1209–1229.
[36] C. Miehe, F. Welschinger, M. Hofacker, Thermodynamically consistent phase-field models of fracture: Variational principles and multi-field FE implementations, Internat. J. Numer. Methods Engrg. 83 (10) (2010) 1273–1311.
[37] L. De Lorenzis, C. Maurini, Nucleation under multi-axial loading in variational phase-field models of brittle fracture, Int. J. Fract. (2021) 1–21.
[38] S.A. Vajari, M. Neuner, P.K. Arunachala, A. Ziccarelli, G. Deierlein, C. Linder, A thermodynamically consistent finite strain phase field approach to ductile fracture considering multi-axial stress states, Comput. Methods Appl. Mech. Engrg. 400 (2022) 115467.
[39] B. Bourdin, C. Chukwudozie, K. Yoshioka, A variational approach to the numerical simulation of hydraulic fracturing, in: SPE Annual Technical Conference and Exhibition, OnePetro, 2012.
[40] A. Mikelić, M.F. Wheeler, T. Wick, A phase-field method for propagating fluid-filled fractures coupled to a surrounding porous medium, Multiscale Model. Simul. 13 (1) (2015) 367–398.
[41] W. Ehlers, C. Luo, A phase-field approach embedded in the theory of porous media for the description of dynamic hydraulic fracturing, Comput. Methods Appl. Mech. Engrg. 315 (2017) 348–368.
[42] C. Maurini, B. Bourdin, G. Gauthier, V. Lazarus, Crack patterns obtained by unidirectional drying of a colloidal suspension in a capillary tube: Experiments and numerical simulations using a two-dimensional variational approach, Int. J. Fract. 184 (1–2) (2013) 75–91.
[43] C. Miehe, S. Mauthe, Phase field modeling of fracture in multi-physics problems. Part III. Crack driving forces in hydro-poro-elasticity and hydraulic fracturing of fluid-saturated porous media, Comput. Methods Appl. Mech. Engrg. 304 (2016) 619–655.
[44] T. Cajuhi, L. Sanavia, L. De Lorenzis, Phase-field modeling of fracture in variably saturated porous media, Comput. Mech. 61 (3) (2018) 299–318.
[45] Y. Heider, W. Sun, A phase field framework for capillary-induced fracture in unsaturated porous media: Drying-induced vs. hydraulic cracking, Comput. Methods Appl. Mech. Engrg. 359 (2020) 112647.
[46] S.H. Ommi, G. Sciarra, P. Kotronis, Variational approach to damage induced by drainage in partially saturated granular geomaterials, Front. Mech. Eng. 8 (2022) 869568, http://dx.doi.org/10.3389/fmech.2022.869568.
[47] K. Pham, J.-J. Marigo, C. Maurini, The issues of the uniqueness and the stability of the homogeneous response in uniaxial tests with gradient damage models, J. Mech. Phys. Solids 59 (6) (2011) 1163–1190.
[48] T. Gerasimov, U. Römer, J. Vondřejc, H.G. Matthies, L. De Lorenzis, Stochastic phase-field modeling of brittle fracture: Computing multiple crack patterns and their probabilities, Comput. Methods Appl. Mech. Engrg. 372 (2020) 113353.
[49] A.A.L. Baldelli, C. Maurini, Numerical bifurcation and stability analysis of variational gradient-damage models for phase-field fracture, J. Mech. Phys. Solids 152 (2021) 104424.
[50] L. Böger, M.-A. Keip, C. Miehe, Minimization and saddle-point principles for the phase-field modeling of fracture in hydrogels, Comput. Mater. Sci. 138 (2017) 474–485.
[51] B. Bourdin, J.-J. Marigo, C. Maurini, P. Sicsic, Morphogenesis and propagation of complex cracks induced by thermal shocks, Phys. Rev. Lett. 112 (1) (2014) 014301.
[52] P. Sicsic, J.-J. Marigo, C. Maurini, Initiation of a periodic array of cracks in the thermal shock problem: A gradient damage modeling, J. Mech. Phys. Solids 63 (2014) 256–284.
[53] A.H.C. Chan, M. Pastor, B.A. Schrefler, T. Shiomi, O.C. Zienckiewicz, Computational Geomechanics: theory and Applications, Wiley, 2022.
[54] O. Coussy, Poromechanics, Wiley, 2004.
[55] O. Coussy, Mechanics and Physics of Porous Solids, Wiley, 2010.
[56] M.T. van Genuchten, A closed-form equation for predicting the hydraulic conductivity of unsaturated soils, Soil Sci. Soc. Am. J. 44 (5) (1980) 892–898.
[57] B.A. Schrefler, D. Gawin, The effective stress principle: Incremental or finite form, Int. J. Numer. Anal. Methods Geomech. 20 (11) (1996) 785–814.
[58] L. Ambrosio, V.M. Tortorelli, Approximation of functional depending on jumps by elliptic functional via t-convergence, Comm. Pure Appl. Math. 43 (8) (1990) 999–1036.

[59] J.-J. Marigo, C. Maurini, K. Pham, An overview of the modelling of fracture by gradient damage models, Meccanica 51 (12) (2016) 3107–3128.
[60] K. Yoshioka, B. Bourdin, A variational hydraulic fracturing model coupled to a reservoir simulator, Int. J. Rock Mech. Min. Sci. 88 (2016) 137–150.
[61] R.M. Lakshmikantha, P. Prat Catalán, A. Ledesma Villalba, Boundary effects in the desiccation of soil layers with controlled environmental conditions, Geotech. Test. J. 41 (4) (2018) 675–697.
[62] H. Zeng, C.-S. Tang, Q. Cheng, C. Zhu, L.-Y. Yin, B. Shi, Drought-induced soil desiccation cracking behavior with consideration of basal friction and layer thickness, Water Resour. Res. 56 (7) (2020) e2019WR026948.
[63] B.A. Schrefler, The Finite Element Method in Soil Consolidation (Ph.D. thesis), University College of Swansea, 1984.
[64] R.I. Borja, On the mechanical energy and effective stress in saturated and unsaturated porous continua, Int. J. Solids Struct. 43 (6) (2006) 1764–1786.
[65] M. Nuth, L. Laloui, Effective stress concept in unsaturated soils: Clarification and validation of a unified framework, Int. J. Numer. Anal. Methods Geomech. 32 (7) (2008) 771–801.
[66] C. Gavagnin, L. Sanavia, L. De Lorenzis, Stabilized mixed formulation for phase-field computation of deviatoric fracture in elastic and poroelastic materials, Comput. Mech. 65 (6) (2020) 1447–1465.
[67] T. Gerasimov, L. De Lorenzis, On penalization in variational phase-field models of brittle fracture, Comput. Methods Appl. Mech. Engrg. 354 (2019) 990–1026.